Longitudinal Combustion Instability in a Rocket Engine with a Single Coaxial Injector

Tuan M. Nguyen,* Pavel P. Popov,† and William A. Sirignano‡
University of California, Irvine, California 92697

DOI: 10.2514/1.B36516

Longitudinal combustion instability in liquid-propellant rocket engines is investigated using an in-house axisymmetric, multispecies compressible flow solver. Turbulence is treated using a hybrid Reynolds-averaged Navier–Stokes/large-eddy simulation approach. The combustion–turbulence interactions are modeled using the flamelet/progress-variable approach. The computational time is at least an order of magnitude smaller than existing axisymmetric simulations with a more detailed chemistry mechanism. Three flow configurations with a choked nozzle are studied: unstable cases with 12 and 14 cm oxidizer post lengths, and a semiunstable case with a 9 cm oxidizer port length. Numerical results for oscillation frequencies and amplitudes agree with the continuously variable resonance combustor experiments conducted at Purdue University. Good agreements with existing computational results are also found. An additional open-end constant-pressure simulation with (otherwise) the same configuration as the continuously variable resonance combustor experiment with the 14 cm oxidizer post is performed, yielding minor acoustic oscillation. The open-end vortex-shedding frequency is found to be roughly one-half of the frequency of vortex shedding calculated in the continuously variable resonance combustor configuration. The flame region compacts as the combustion chamber becomes more unstable. The choked nozzle allows large-amplitude oscillation, thereby enhancing mixing and leading to more complete combustion near the pressure antinode (combustion chamber entrance) as compared to the open-end chamber. Pulse timing in the unstable case is identified as a major factor for the instability mechanism. Oscillatory behaviors for all three instability domains are described.

Nomenclature

C	=	progress variable
C_χ	=	proportionality constant between turbulence and scalar timescales
c_p	=	specific heat capacity at constant pressure
E	=	total energy
h	=	enthalpy
k	=	turbulent kinetic energy
P	=	probability density function
Pr_t	=	turbulent Prandtl number
p	=	pressure
Sc_t	=	turbulent Schmidt number
T	=	temperature
t	=	time
v_i/v_j	=	velocity vector
x_i/x_j	=	spatial vector
Z	=	mixture fraction
Z''^2	=	mixture fraction variance
γ	=	ratio of specific heat capacity
λ	=	thermal diffusivity
μ	=	dynamic molecular viscosity
μ_t	=	turbulent/eddy viscosity
ρ	=	density
τ_{ij}	=	viscous stress tensor
τ_{ij}^R	=	Reynolds stress tensor
ψ	=	arbitrary scalar
ω	=	turbulent frequency
$\bar{}$	=	Reynolds average
$\tilde{}$	=	density-weighted Favre average

Received 25 October 2016; revision received 2 June 2017; accepted for publication 29 June 2017; published online 28 August 2017.

*Graduate Research Assistant, Department of Mechanical and Aerospace Engineering. Student Member AIAA.

†Postdoctoral Researcher, Department of Mechanical and Aerospace Engineering; currently Researcher, University of Illinois at Urbana–Champaign, Champaign, IL 61820. Member AIAA.

‡Professor, Department of Mechanical and Aerospace Engineering. Fellow AIAA.

I. Introduction

COMBUSTION instability is an acoustical phenomenon in which combustion excites and sustains an unstable pressure oscillation. It occurs in most major high-power propulsion systems that propel rockets and airplanes. These systems have a high-energy release rate with relatively low losses, which in turn reinforce acoustical oscillations with very high amplitudes. These oscillations can cause undesirable effects on thrust, and sometimes engine destruction.

Combustion instability has been continuously studied since its discovery, with emphasis being shifted depending on the systems. In the United States, elimination of high-frequency resonance burning (a term widely accepted back then) in small tactical solid rocket motors was the main research focus during World War II. Installations of baffles, resonance rods, or some modifications of geometry were found to be the solutions.

During the 1960s and the Apollo program, combustion instabilities found in the F1 liquid rocket engine became a major issue. Similar to the solutions for solid rocket motors, installations of baffles were found to stabilize the engine [1]. Combustion instabilities have also been found in jet-engine afterburners [2], with high-frequency transverse modes similar to oscillations found in liquid rockets. With modifications to the geometry, especially for high bypass engines, these transverse modes were replaced by lower-frequency longitudinal vibrations. Similarly, transverse combustion instabilities found in liquid-fueled ramjets were treated with more compact designs, causing longitudinal oscillations with lower frequencies.

Longitudinal instability, often with much lower oscillation frequencies than its transverse counterpart, cannot simply be treated by installation of baffles or modifications of geometry. Therefore, our goal is to understand the causes of longitudinal combustion instability and possible means of treatment. Culick [3] noted that there were two types of acoustical combustion instability: driven and self-excited. Driven combustion instability is more relevant in solid-propellant rocket engines. Self-excited instabilities can be found mostly in liquid-propellant rockets. There are two types of

self-excited instabilities: linear and nonlinear behaviors. Linear behavior refers to spontaneous instability. In this case, oscillations are excited and grow to an unstable high amplitude from normal noises. Nonlinear behaviors, on the other hand, refer to any instability triggered by unusual conditions such as irregular flow rates, or large acoustic disturbances. These disturbances need to have sufficient magnitude to overcome the required threshold [4]. Although the technical terms refer to two different kinds of instabilities, both types exhibit nonlinear behaviors once they are excited. In this paper, we will concern ourselves with spontaneous instability.

In the 1950s and 1960s, linear behavior received widespread attention. Comprehensive compilation of works edited by Harrje and Reardon [5] should be reviewed for a complete picture. Early prominent theoretical work on longitudinal mode linear instability was addressed extensively by Crocco and Cheng [6,7]. These works laid the early theoretical foundations describing combustion response and reinforcement of acoustic oscillations within liquid-propellant rocket engine using sensitive time lag theory. The two parameters (n, τ) were introduced, where n was the pressure index of interaction, whereas τ represented the pressure-sensitive time lag [6]. For a certain discrete range of values of τ at a natural frequency (mode), a system is unstable if n is greater than a certain minimum limit. Based on this conclusion, longitudinal oscillations with the effect on mass, momentum, and energy exchanged between phases were established. Because the two parameters n and τ were independent of oscillation frequency, a description of the unsteady combustion process can be avoided. Sirignano and Crocco [8] and, later, Mitchell et al. [9] performed nonlinear analyses for the longitudinal mode with both spontaneous and triggered instabilities while also allowing shock waves to develop. These pioneering works were limited to theoretical perturbation analysis.

Since these early pioneering works, various levels of research from experimental [10–12] to analytical [13–15] works have been conducted. Numerical models describing different phenomena in combustion instabilities have been established [4,16–19]. With recent advancements of computer architectures, there are also renewed interests in studying both transverse and longitudinal combustion instabilities via high-fidelity numerical simulations [20–24]. These simulations demonstrated the ability to correctly capture complex physical phenomena found in various experiments. Additionally, they quantified the flowfield in both the spatial and time domains, which is not easily captured using experimental techniques. However, most of these simulations are computationally expensive. These works use either large-eddy simulation (LES) or a hybrid Reynolds-averaged Navier–Stokes (RANS)/LES method to treat turbulence. The turbulence–chemistry interaction has been treated by solving species transport equations with modeled reaction source terms. The resulting system of equations is not only numerically stiff but also computationally expensive. Most of these existing computations were run with thousands of cores. Furthermore, because of the expensive grid restrictions of three-dimensional (3-D) LES computations, most of these calculations are limited to either one- or two-step reaction mechanisms. Many of these simulations took weeks or, in some cases, months to complete.

Therefore, the first objective in this work is to develop a computationally inexpensive numerical tool. The developed tool is benchmarked against not only experimental results but also existing numerical simulations to validate its ability to capture the correct physical phenomena. In surveying a suitable experiment, a series of longitudinal combustion instabilities experiments conducted at Purdue University (Purdue) was found [25–28]. Using a scaled combustion chamber with a single injector, these experiments provided detailed measurements of the mixing and reactions occurring in the combustion flowfield. Moreover, a careful injector/combustion chamber acoustical design allows the system to sustain and amplify any resulting small-pressure disturbance (rumbling noise) [25]. Different stability domains were found in the continuously variable resonance combustor (CVRC) experiments by varying the oxidizer post lengths from 9 to 19 cm. Existing computational results using various turbulence and combustion models for these experiments are available [23,29–32]. Srinivasan et al. [23] studied the flame dynamics of different stability domains using a LES turbulence model coupled with a linear eddy mixing combustion model. Comparing different oxidizer post lengths, the authors found different stability domains that were consistent with the experiments. They concluded that acoustic interactions with the flowfield led to subtle changes in the vorticity (and mixing dynamics) between these cases. Premixed and non-premixed burnings were found to coexist within the chamber. Garby et al. [29] studied both axisymmetric and fully 3-D flame stabilization mechanisms for the 12 cm oxidizer post using a LES method coupled with a dynamic flame thickened chemistry model. They demonstrated that, although the axisymmetric flame simulation qualitatively captured the unstable behavior, it underpredicted the oscillation magnitudes as compared to both 3-D and experimental results. Harvazinski et al. [30] studied the effects of grid resolution and dimensionality on the ability to predict combustion instability using both axisymmetric and 3-D simulations using a detached-eddy simulation (DES) turbulence model with laminar closure model for chemistry. They performed three different simulations: one 3-D, and two axisymmetric with two different grid sizes. Similar to Garby et al. [29], the 3-D results matched the experimental data very well. On the other hand, their axisymmetric simulations underpredicted the oscillation magnitudes by 50–60%. In all three studies, the simulations overpredicted the oscillations frequency. All of the authors postulated that, by using the adiabatic wall boundary condition, the flames in these simulations were hotter as compared to the experiments, thus leading to a rise in the mean chamber pressure and the speed of sound.

Based on these findings, a new code is written using an axisymmetric formulation. As shown by Garby et al. [29], the axisymmetric flame length is significantly longer than the 3-D result due to the effect of imposing the zero-gradient turbulent boundary condition on the axis of symmetry. The lack of vortex stretching and tilting in axisymmetric calculations also means turbulence structures generated by axisymmetric calculations are different than those of 3-D simulations. These effects lead to different mixing and burning characteristics between axisymmetric and 3-D calculations. However, as shown in various calculations [23,29], the major instability characteristics of the CVRC experiments occur in the longitudinal direction. Therefore, the neglect of the third direction is justified with regard to capturing the wave dynamics. As shown in various axisymmetric calculations of the CVRC experiments [32,33], the DES turbulence model can be used to qualitatively capture the correct physics. Near a wall, the model behaves the same as a RANS model. Far away from the wall, the turbulent viscosity values decrease significantly as compared to a traditional RANS model, allowing it to behave as a subgrid model, just like a LES [34]. The RANS feature of DES alleviates the major difficulty associated with a LES, where either a wall model or extremely fine grid must be used near the walls. DES is therefore a less expensive treatment of turbulence as compared to the LES. In our code, an improved version of the Wilcox $k-\omega$ DES model called delayed detached-eddy simulation (DDES) is implemented. Harvazinski et al. [31] performed 3-D simulations using a detailed chemistry mechanism (GRI-Mech 1.2). The same oscillation magnitudes were observed as compared to calculations with global chemistry mechanisms. On the other hand, Sardeshmukh et al. [33] showed that, by using the same detailed chemical mechanism as Harvazinski et al. [31] (GRI-Mech 1.2), their DES axisymmetric simulation could capture much a larger oscillation amplitude (80–90% of the experimental results) as compared to calculations using global mechanisms. Both Sardeshmukh et al. [33] and Harvazinski et al. [31] used the laminar closure combustion model, in which the transport equations for all species were solved. The computational costs associated with these calculations are thus prohibitively expensive. Therefore, the flamelet/progress variable (FPV) is chosen in our study for its ability to incorporate complex detailed mechanisms while maintaining inexpensive computational costs.

In the following sections, the governing equations are presented. The choice of the DDES turbulence model over unsteady RANS is explained. Details of the FPV approach are described, and the flamelet solutions are examined. A sample solution of the temperature

flamelet library is also presented. Details of the numerical cost of the new code will be compared with existing simulations. Our results are then benchmarked against existing experimental and numerical data. The results of an additional simulation with an open-end exit boundary condition are also presented. Three different instability domains for different cases are found. Several characteristics of the experimental rigs, such as pressure wave spatial mode shape, time-averaged behaviors, flames, and vortex dynamics, are discussed.

II. Numerical Framework

A. Governing Equations

For a multispecies mixture, the Favre-averaged Navier–Stokes equations are written in conservative form as follows [35]:

$$\frac{\partial \bar{\rho}}{\partial t} + \frac{\partial \bar{\rho}\tilde{v}_j}{\partial x_j} = 0 \tag{1}$$

$$\frac{\partial \bar{\rho}\tilde{v}_i}{\partial t} + \frac{\partial \bar{\rho}\tilde{v}_i\tilde{v}_j}{\partial x_j} = -\frac{\partial \bar{p}}{\partial x_i} + \frac{\partial(\tau_{ij} + \tau_{ij}^R)}{\partial x_j} \tag{2}$$

$$\frac{\partial \bar{\rho}\tilde{E}}{\partial t} + \frac{\partial \tilde{v}_j(\bar{\rho}\tilde{E} + \bar{p})}{\partial x_j} = \frac{\partial}{\partial x_j}\tilde{v}_i(\tau_{ij} + \tau_{ij}^R) + \mu + \sigma_k\mu_t\frac{\partial k}{\partial x_j} + \frac{\partial}{\partial x_j}\frac{\lambda}{c_p} + \frac{\mu_t}{Pr_t}\frac{\partial \tilde{h}}{\partial x_j} \tag{3}$$

The total energy $\tilde{E}$ has the form of

$$\tilde{E} = \frac{1}{2}\sum_{j=1}^{n} v_j v_j + k + \tilde{e}$$

where n is the number of dimensions. The first term on the right-hand side is the mean flow kinetic energy. The second term is the turbulent kinetic energy k. Note that $\tilde{e}$ is the total thermal energy, which includes the sensible and chemical energies. Enthalpy $\tilde{h}$ is related to the total thermal energy as $\tilde{h} = \tilde{e} + \bar{p}/\bar{\rho}$. For high-pressure combustion, the ideal gas law is assumed ($\bar{p} = \bar{\rho}R\tilde{T}$), where R is the specific gas constant. The turbulent Schmidt Sc_t and Prandtl (Pr_t) numbers are assumed to be constant at 0.9.

B. Turbulence Model

Here, the original turbulence model chosen was the 2006 Wilcox $k-\omega$ model [36]. The $k-\omega$ model and its variations work very well with internal flow, as opposed to its $k-\epsilon$ counterpart, which does not accurately solve separated flows under adverse pressure gradients. The conservative forms of the governing equations for k and ω are written as follows [36]:

$$\frac{\partial \bar{\rho}k}{\partial t} + \frac{\partial(\bar{\rho}\tilde{v}_j k)}{\partial x_j} = (\tau_{ij} + \tau_{ij}^R)\frac{\partial \tilde{v}_i}{\partial x_j} - \beta^*\bar{\rho}\omega k + \frac{\partial}{\partial x_j}\mu + \sigma_k\frac{\rho k}{\omega}\frac{\partial k}{\partial x_j} \tag{4}$$

$$\frac{\partial \bar{\rho}\omega}{\partial t} + \frac{\partial(\bar{\rho}\tilde{v}_j\omega)}{\partial x_j} = \frac{\gamma\omega}{k}(\tau_{ij} + \tau_{ij}^R)\frac{\partial \tilde{v}_i}{\partial x_j} - \beta\bar{\rho}\omega^2 + \frac{\partial}{\partial x_j}\mu + \sigma_\omega\frac{\bar{\rho}k}{\omega}\frac{\partial \omega}{\partial x_j} + \frac{\bar{\rho}\sigma_d}{\omega}\frac{\partial k}{\partial x_j}\frac{\partial \omega}{\partial x_j} \tag{5}$$

where β^*, β, σ_k, σ_ω, and σ_d are modeling constants. The turbulent viscosity is calculated as $\mu_t = \bar{\rho}k/\hat{\omega}$, where $\hat{\omega}$ is the turbulent frequency corrected by the maximum of ω and the flow mean strain rate.

Our own unpublished computations show that RANS turbulence models in general overproduce turbulent viscosity. The large turbulent viscosity dampens any unsteady motion of the fluids: particularly, vortex shedding and acoustic wave propagation. The inherent problem arises from the incorrect assumption that all scales of the unsteady motion can be captured by the turbulence model.

One remedy is to modify the RANS model so that the computed turbulent viscosity does not capture any grid-resolved turbulent scales. This approach is a hybrid RANS/LES approach that incorporates aspects of both turbulence models. The approach is called detached-eddy simulation, which was first proposed by Spalart et al. [34] for the one-equation Spalart–Allmaras turbulence model. Strelets [37] expanded the concept to Menter's shear stress transport $k-\omega$ model. An improved version of the DES model called delayed detached-eddy simulation, which limits the grid arbitrariness, is implemented here.

The dissipation term in Eq. (4) (second term on the right-hand side) is modified to exclude any grid-realized contribution in the turbulent viscosity. This can be achieved using the mathematical definition $\beta^*\rho\omega k = \rho k^{3/2}/L_T^*$. The corrected turbulent length scale is defined as $L_T^* = \min(L_T, C_{\mathrm{DES}}L_{\mathrm{GRID}})$, where C_{DES} is a modeling constant. L_T and L_{GRID} are the turbulent and grid length scales where $L_T = k^{1/2}/(\beta^*\omega)$ and $L_{\mathrm{GRID}} = L_T - F_D(L_T - \Delta)$. Δ is the largest grid dimension for the cell. F_D is a blending function that eliminates the grid-size arbitrariness by determining the location of the cell away from the wall: $F_D = 1 - \tanh[(1.5L_T/d_{\mathrm{wall}})^3]$, where d_{wall} is the shortest distance of any given cell from any wall in the computational domain.

C. Turbulent Combustion Model

The flamelet concept, as a class of turbulent combustion modeling, was first introduced by Peters [38]. It assumes the chemical timescales are shorter than the turbulence timescales in the energy-containing eddies so that the flame can be approximated as one-dimensional. Therefore, turbulent flames are collections of laminar flame elements embedded in and interacting with the turbulent flowfield. The local flame structure is similar to those of laminar flamelets. Detailed chemical mechanisms can be incorporated while retaining low computational cost. The FPV approach was originally developed for incompressible (constant pressure) flow [39]. However, it was since applied successfully to compressible flow with various turbulence models. Pecnik et al. [35] and Saghafian et al. [40] studied high-speed supersonic combustion in scramjets using the FPV method coupled with RANS and LES turbulence models. Wang et al. [41] successfully simulated supersonic combustion in the DLR (German Aerospace Center) and Gamba combustors using the FVP approach with the improved delayed detached-eddy simulation turbulence model.

In any flamelet approach, the laminar flamelet solutions are first solved using the flamelet equations [38]. However, in a RANS-based turbulence code such as ours, we can only transport mean quantities. Subsequently, the laminar flamelet solutions are convoluted with assumed probability density functions (PDFs) of independent scalars such as the mean mixture fraction $\tilde{Z}$ and the mean variance Z''^2. The convolution creates a series of flamelet libraries that can be quickly accessed during the computational fluid dynamics (CFD) computations, thus allowing us to maintain low computational cost. Furthermore, in the FPV approach, the flamelet libraries are also parameterized by a mean reaction progress variable $\tilde{C}$:

$$\tilde{\psi}_i(\tilde{Z}, \tilde{Z''^2}, \tilde{C}) = \int_0^1\int_0^1 \psi_i(Z, C)\tilde{P}(Z, Z''^2, C)\,\mathrm{d}Z\,\mathrm{d}C \tag{6}$$

In Eq. (6), $\tilde{P}$ is the PDF function. The PDF for the progress variable C is assumed to be the Dirac δ function; thus, Eq. (6) is reduced to

$$\tilde{\psi}_i(\tilde{Z}, \tilde{Z''^2}, \tilde{C}) = \int_0^1 \psi_i(Z, \tilde{C})\tilde{P}(Z, Z''^2)\,\mathrm{d}Z$$

The β PDF is assumed as

$$\tilde{P}(Z, Z''^2) = \frac{Z^{\alpha-1}(1-Z)^{\beta-1}}{\Gamma(\alpha)\Gamma(\beta)}\Gamma(\alpha+\beta)$$

where Γ is the gamma function. The shape functions α and β are related to the mixture fraction and its variance by $\alpha = Z\gamma$; and $\beta = (1 - Z)\gamma$, with $\gamma = ((Z(1 - Z))/Z''^2) - 1 \geq 0$.

For compressible flow, these libraries are also generated at different background pressures. Therefore, the flamelet libraries are parameterized by the three scalars $\tilde{Z}$, $\widetilde{Z''^2}$, $\tilde{C}$ as well as the pressure p.

During the CFD computation, the transport equations for the scalars $\tilde{Z}$, $\widetilde{Z^2}$, and $\tilde{C}$ are solved. The mean mixture fraction squared $\widetilde{Z^2}$ is related to the mean mixture fraction and the mean variance as $\widetilde{Z^2} = \tilde{Z}^2 + \widetilde{Z''^2}$.

At each time step, the local values of these scalars along with the pressure allow us to quickly retrieve properties such as local compositions, temperature, specific heat c_p, enthalpy, and thermal diffusivity using pretabulated flamelet libraries. When the Lewis number equals to one, the transport equations for these scalars are given as

$$\frac{\partial \bar{\rho}\tilde{Z}}{\partial t} + \frac{\partial \bar{\rho}\tilde{v}_j\tilde{Z}}{\partial x_j} = \frac{\partial}{\partial x_j}\left[\frac{\lambda}{c_p} + \frac{\mu_t}{Sc_t}\frac{\partial \tilde{Z}}{\partial x_j}\right] \tag{7}$$

$$\frac{\partial \bar{\rho}\widetilde{Z^2}}{\partial t} + \frac{\partial \bar{\rho}\tilde{v}_j\widetilde{Z^2}}{\partial x_j} = \frac{\partial}{\partial x_j}\left[\frac{\lambda}{c_p} + \frac{\mu_t}{Sc_t}\frac{\partial \widetilde{Z^2}}{\partial x_j}\right] - \bar{\rho}C_x\omega(\widetilde{Z^2} - \tilde{Z}^2) \tag{8}$$

$$\frac{\partial \bar{\rho}\tilde{C}}{\partial t} + \frac{\partial \bar{\rho}\tilde{v}_j\tilde{C}}{\partial x_j} = \frac{\partial}{\partial x_j}\left[\frac{\lambda}{c_p} + \frac{\mu_t}{Sc_t}\frac{\partial \tilde{C}}{\partial x_j}\right] + \dot{\tilde{\omega}}_C \tag{9}$$

where C_x has a constant value of 2.0 [35].

D. Numerical Details

1. Numerical Scheme

The developed numerical tool is a multiblock, finite difference structured code written in cylindrical formulation. Overall, the code is second-order accurate in space and fourth-order accurate in time. Spatial domains are discretized with central differencing for both convection and diffusion terms. Jameson's hybrid second-/fourth-order artificial viscosity is added to stabilize the convective terms [42] and enable shock-capturing capability. Shock-wave formation has been observed in longitudinal mode oscillations. Thus, an ability to capture shocks in the numerical analysis is important. A low-storage fourth-order Runge–Kutta time-integration scheme, which allows a Courant–Friedrichs–Lewy number of 1.8, is implemented [43]. More details of the numerical scheme and the overall implementation are given in the appendices.

2. Computational Domain

Figure 1 shows the computational domain related to the CVRC experiment. The experimental configuration is essentially a dump combustor with a central oxidizer post and a coaxial fuel post. The two propellant streams start to mix at the end of a splitter plate, 1 cm upstream of the combustion chamber dump plane. In the CVRC experiments, a pressure tap is installed on the combustion chamber wall at $x = 37$ cm. This point will be used as a benchmarking location with both experimental and other existing computational results.

3. Boundary Conditions

As observed in the existing computational results [23,29], the adiabatic wall boundary condition leads to higher mean chamber pressure, possibly due to hotter flame, thus resulting in higher values of pressure oscillation frequencies as compared to the experimental values. There is, however, a limited number of studies using either an isothermal or imposed heat transfer wall. Harvazinski et al. [32] numerically simulated the CVRC experiments using constant-temperature wall boundary conditions for the chamber wall at four different temperatures: 300, 600, 900, and 1200 K. At 300 and 600 K, no combustion was observed. At 900 and 1200 K, stabilized combustion occurred with lower-pressure oscillation magnitude; the cooler wall temperature had a greater stabilizing effect. Srinavasan et al. [23] observed a similar trend while showing that the constant-temperature walls only changed the oscillation magnitude and not the overall stable characteristics. Therefore, in the first step validating a newly developed code, the adiabatic wall treatment is used. Additionally, the walls have no slip and are impermeable.

A constant mass flow rate inlet boundary condition is implemented using the Navier–Stokes characteristic boundary conditions [44]. To save computational resources, a short-choked-nozzle [45] outlet boundary condition is used instead of an actual convergent–divergent nozzle computational domain. The entrance-to-throat area ratio is five, based on the CVRC experimental geometry. An open-end exit boundary condition with constant pressure is also used to compare the vortex structures in the case of a low-amplitude oscillation against the high-oscillation amplitude for the CVRC experiment. The propellant mass injection rates are the same in both the open-end and choked-nozzle cases.

The gaseous oxidizer consists of 58% water (H_2O) and 42% oxygen (O_2) by mass, with an inlet temperature of 1030 K. The fuel is gaseous methane with an inlet temperature of 300 K. The mass flow rates are $\dot{m}_{ox} = 0.32$ kg/s and $\dot{m}_f = 0.027$ kg/s for the oxidizer and fuel, respectively. The flow is thus globally fuel lean with an equivalent ratio of 0.8.

4. Initial Condition

The initial conditions are modeled to enhance ignition and quickly establish the operating condition. At time $t = 0$, the flow in the computational domain is filled with quiescent hot products ($T = 2700$ K). The hot products ensure that the cold reactants can simultaneously combust. A hyperbolic tangent ramp function in the form of

$$\dot{m} = \dot{m}_i/2[\tanh(2k_0(t - t_0)) + 1]$$

gives a sufficiently slow transition for the injection of the propellants into the computational domain, where t has a unit of milliseconds; k_0 and t_0 are constants taken as 0.1 and 2.5 ms, respectively; and $\dot{m}_i$ is either the steady-state fuel or oxidizer mass flow rate. The duration of injection is 4 ms. After the reactants are fully injected, the mass flow rates are kept constant, as previously described.

III. Results

A. Flamelet Solutions

The laminar flamelet solutions are obtained using the FlameMaster code [46]. A 72-reaction detailed mechanism with 27 species (neglecting nitrogen) is used [47].

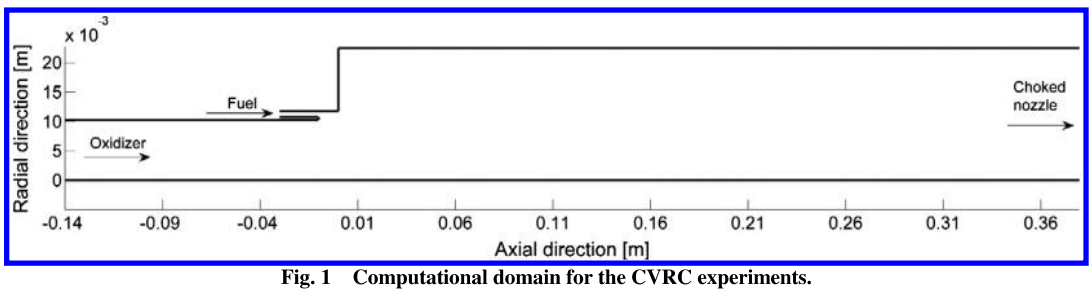

Fig. 1 Computational domain for the CVRC experiments.

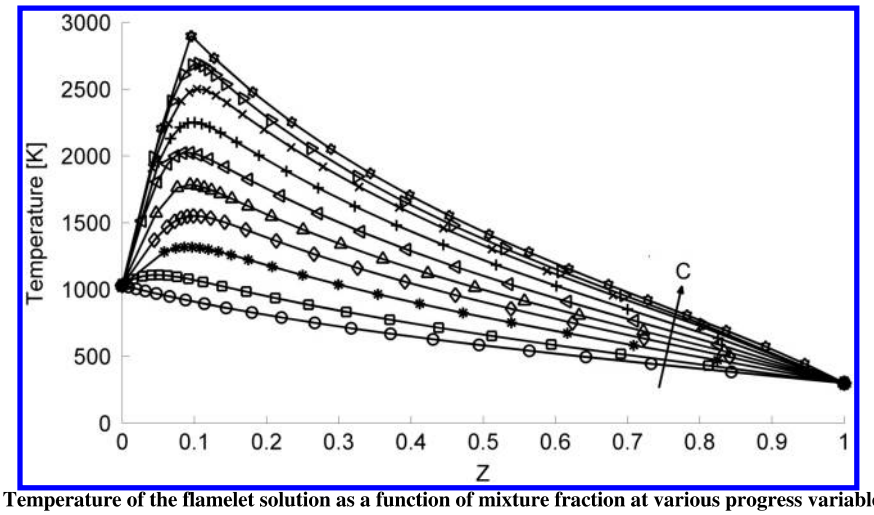

Fig. 2 Temperature of the flamelet solution as a function of mixture fraction at various progress variable values.

In existing literature, H_2O is commonly chosen as the progress variable. However, because the oxidizer inflow already contains some water vapor, the progress variable is taken as the total mass fraction of H_2 and CO_2. Figure 2 illustrates the use of the progress variable in our computation. The bottom curve indicates a mixing solution, where the progress variable is equal to zero. As the flow starts to react, more products including the progress variable are produced (indicated by the bottom-right arrow). This point is further illustrated by the increase in flame temperatures for subsequent curves.

B. Assessment of the Computational Cost

Initially, the computational domain only contains hot products under quiescent conditions. As previously mentioned, both the fuel and oxidizer are slowly injected into the computational domain. After the flow is fully established, each simulation is run for an additional 70 ms, or more than 100 first-mode longitudinal cycles. Finally, data are analyzed using the last 20 ms, corresponding to roughly 28–30 cycles.

As previously mentioned, a purpose of this work is to develop a computationally efficient numerical tool. Table 1 compares the computational cost between our work here at the University of California, Irvine (UCI) and other various simulations performed by different groups.

As seen in Table 1, most of these simulations use either a global one- or two-step chemical mechanism. The same code, called the general equation and mesh solver (GEMS), is used at both Purdue University and the U.S. Air Force Research Laboratory (AFRL), which can perform both 3-D and axisymmetric simulations Harzavinski [48]. Furthermore, the GEMS solver employs a similar turbulence model used in this work: the Wilcox $k-\omega$-based DES model. The simulation performed at the CNRS employed the classical Smagorinsky LES turbulence model. Both axisymmetric and 3-D simulations were performed. Although it was concluded in these simulations that axisymmetric calculations were at least an order of magnitude cheaper than its 3-D counterpart, they could qualitatively reproduce some feature of the instability. The axisymmetric calculations, however, underpredict the oscillation amplitude by 20–50%.

Table 1 shows that our computational cost per millisecond of physical time is by far the least expensive: even when compared to existing axisymmetric calculations. The reasons for such low computational costs can be explained on two fronts. First, the time-integration scheme used here is an explicit scheme. The solvers employed at Centre National de la Recherche Scientifique (CNRS) and the Georgia Institute of Technology (Georgia Tech) both used variations of the explicit predictor–corrector time-integration scheme. The GEMS code, on the other hand, employed a fully implicit scheme. Evidently, the computational costs for all the GEMS code simulations are always higher. Second, the turbulent combustion model employed in this work used a series of flamelet libraries, or preprocessed lookup tables. There are only three transport equations [Eqs. (7–9)] solved for the chemistry, regardless of the chemical mechanisms used. In comparison, even the simplest global chemical mechanisms required at least four transport equations (two reactants and two products). Therefore, the associated cost with calculating the flow thermodynamics properties at the end of each time step is greatly reduced.

Two different mesh sizes of 60,000 grid points and 82,000 grid points were used for the most unstable cases of the CVRC experiments. Flame dynamics time-averaged flowfield analyses revealed small differences between the two mesh sizes. Moreover, a true grid convergence study for a relatively new turbulence model such as DES or even LES using even the most established codes is a difficult subject on its own [49–51]. Beside the computational cost associated with using finer meshes, different mesh sizes will generate different turbulence structures. Therefore, a rigorous mesh convergence study is a project on its own and can be considered in the future.

Harzavinski [48] showed that, by employing a relatively coarse mesh of roughly 55,000 cells, axisymmetric simulations can still reasonably capture the correct unstable behaviors of the CVRC experiments while underpredicting the oscillation magnitudes by a factor of two or more. Therefore, to efficiently evaluate the ability of the newly written code in capturing the correct physics, the mesh size of roughly 60,000 grid points is used for all the cases presented in the following sections.

Table 1 Computational cost for various simulations of the CVRC experiment

Institution	Type	Mesh size	Number of species	Core hours per millisecond
UCI	Axisymmetric	6.26 – E4	27	0.28
CNRS [29]	Axisymmetric	7 – E5	5	160
Purdue [48]	Axisymmetric	5.5 – E4	4	53
Purdue [48]	Axisymmetric	2 – E5	4	480
CNRS [29]	3-D	14 – E6	5	1,024
AFRL [24]	3-D	4 – E6	4	11,520
AFRL [24]	3-D	4 – E6	31	259,200
Georgia Tech [23]	3-D	1.4 – E6	5	3,333

C. Computational Validation

In the CVRC experiment, the combustion chamber has a fixed length of 38 cm. The oxidizer post length is continuously varied from 19 to 9 cm. Three different cases of the CVRC experiment are used to benchmark against our computational results. These cases correspond to various oxidizer post lengths: 9, 12, and 14 cm. In these cases, the short-choked-nozzle boundary condition is applied. We expect that the experiment with a finite length for the convergent portion of the nozzle should have a lower frequency.

Table 2 shows the first three dominant frequencies. The table also presents comparisons with experimental data as well computational results by Srinivasan et al. [23]. For the 12 and 14 cm oxidizer post, our results generally overpredict the dominant frequencies as compared to the experimental results. However, this trend is consistent with existing computational results. For the 9 cm oxidizer post, our results for the first dominant frequency as well as oscillation amplitude match the experimental results extremely well, whereas Srinivasan et al. overpredicted both quantities. It is possible that the higher frequency is predicted because the wave dynamics depends on a sound speed determined on the resolved scale where larger temperatures occur.

Figure 3 compares the pressure oscillations amplitude for the three reported cases. The sampling location is on the combustion chamber wall before the entrance of the convergent nozzle ($x = 37$ cm). These signals are passed through a bandpass-filtered centered around their respected first-frequency mode identified during the PSD analyses. The time is zeroed by an arbitrary time t_o after the flow has reached the limit cycle.

For the 9 cm oxidizer post length, the chamber is observed as semistable, with the peak-to-peak pressure oscillation of 200 kPa. For the 12 cm oxidizer post length, the system is unstable, with a peak-to-peak amplitude of 450 kPa. The 14 cm post length exhibits similar behavior but with a much larger peak-to-peak amplitude of 600 kPa. In the unstable cases, these results underpredicted the pressure oscillation magnitude by 15–20% as compared to experimental data. On the other hand, 3-D calculations underpredicted the oscillation magnitude within 10% of the experimental data [23,24,29]. Our results, however, predict larger peak-to-peak oscillation amplitudes as compared to existing axisymmetric calculations using global chemistry mechanisms [29,33].

Figure 4 compares the first longitudinal mode shape results of the present work as well as the work of Srinivasan et al. [23]. The results are obtained by computing the modulus of the pressure oscillations (modP') via Fast Fourier Transform analyses at each spatial point along the centerline. For the unstable cases, our results generally agree with the existing computational results. The correct mode shape found in these cases further validates our usage of the exit boundary condition, as the nozzle entrance should behave as a pressure antinode.

Similar to existing simulations, overpredictions of oscillation frequencies in the unstable cases can attribute to the usage of adiabatic boundary conditions, which leads to a much higher mean chamber pressure and increase in the sound speed [23,29]. Figure 5 shows the time-averaged heat release rate for all three cases. For the unstable cases, the flames quickly expand radially downstream of the dump plane. On the other hand, most of the reactions concentrate around the shear layer in the 9 cm oxidizer post case. Therefore, it can be argued that the adiabatic wall boundary condition has less of an effect in the 9 cm oxidizer post case as compared to the unstable cases. This phenomenon results in a lower mean chamber pressure as compared to the unstable cases, in addition to the lower oscillation amplitude. A second explanation can also be found in Fig. 4 In Srinivasan et al.'s results [23], there are clearly half-wave standing waves present in the chamber, with a pressure node at $x = 20$ cm, and there is a pressure antinode immediately downstream of the dump plane ($x = 5$–6 cm) and at the entrance of the nozzle ($x = 38$ cm) for all oxidizer post lengths. This means the full traveling pressure wavelength is about 0.62–0.66 m for the unstable cases. The volume- and time-averaged sound speed in the chamber for the 14 cm post is around 1080 m/s, leading to a theoretical frequency of around 1600 Hz. The 10% difference as compared to the value reported in Table 2 is due to the influence of the bulk velocity. In our results for the 9 cm oxidizer post, there is no distinct pressure antinode downstream of the dump plane. This means the traveling pressure wave in the chamber is simply reflected off the backstep wall. The full wavelength in this case is therefore 0.76 m, with the volume- and time-averaged acoustical speed of 1077 m/s. The calculated frequency is therefore around 1417 Hz, which agrees well with the values reported in Table 2. This analysis only offers a small explanation into the discrepancies between the predicted oscillation frequencies.

D. Instability Mechanisms and Vorticity Dynamics

In the CVRC experiments, the choked nozzle behaves acoustically similar to a closed end. Therefore, to understand the flame and vortex dynamics under natural oscillations, an additional case following the CVRC experimental setup but with a constant-pressure exit boundary condition is used. The oxidizer post length for this constant-pressure case is 14 cm. All other parameters, such as fuel and oxidizer mass flow rates, are kept the same. Therefore, we will only consider three cases: 9 cm post length with choked nozzle outlet (9C), 14 cm post length with choked nozzle outlet (14C), and 14 cm post length with constant-pressure outlet (14CP). These cases correspond to three different stability domains: stable (14CP), semistable (9C), and high-amplitude unstable (14C). The 12 cm post length with a choked nozzle outlet will not be presented because it exhibits similar behavior to case 14C but at a lower-pressure amplitude.

Figure 6 compares pressure oscillation amplitudes for all three cases. There is a significant drop in pressure oscillation amplitudes from case 14C to 14CP. Case 14CP is qualitatively more stable than case 9C.

For case 14CP, the pressure oscillation frequency is 800 Hz. Based on the calculated frequency, Fig. 7 shows the first longitudinal mode shape and its corresponding phase for case 14CP. A quarter-wave standing mode is found in the combustion chamber. The dump plane remains a pressure antinode, whereas the exit is now a pressure node due to the constant-pressure exit condition.

Harvazinski et al. [24] identified three different instability mechanisms in an unstable cycle for the CVRC experiments: triple flame, baroclinic torque, and pulse timing. These mechanisms should not be viewed as the root causes of the self-excited unstable behaviors. The different behaviors are coupled with twoway influences. So, there is no way to distinguish causes and effects. They are, however, important characteristics within an unstable cycle. The triple flame, which is a phenomenon in which two different

Table 2 Dominant frequencies on the combustion chamber wall at x 0.37 cm

Oxidizer post length	First mode, Hz	Second mode, Hz	Third mode
9 cm:-computation (UCI)	1400	2900	4350
9 cm: computation (Srinivasan et al. [23])	1686	2791	3373
9 cm: experiment	1392	2704	3772
12 cm: computation (UCI)	1600	2906	4500
12 cm: computation (Srinivasan et al. [23])	1613	3268	4881
12 cm: experiment	1385	2777	4169
14 cm: computation (UCI)	1520	2880	4440
14 cm: computation (Srinivasan et al. [23])	1592	3130	4722
14 cm: experiment	1331	2655	3986

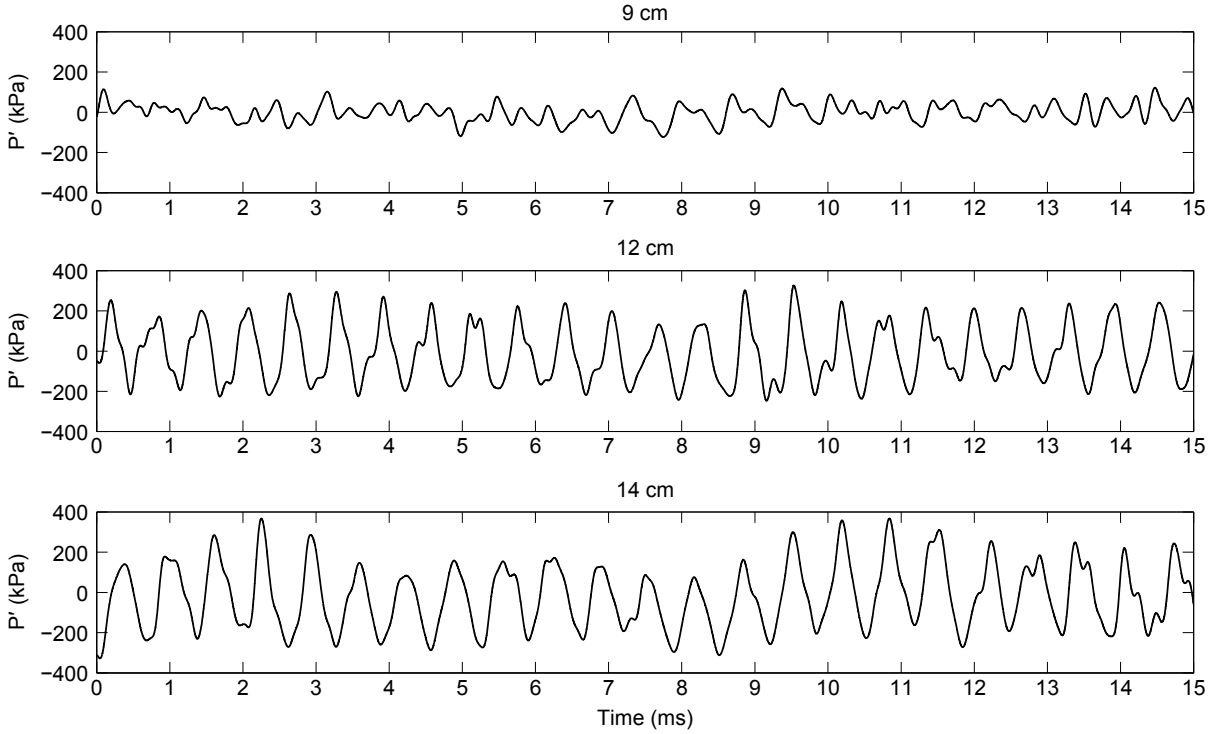

Fig. 3 Time evolution of the pressure signals for various oxidizer post lengths.

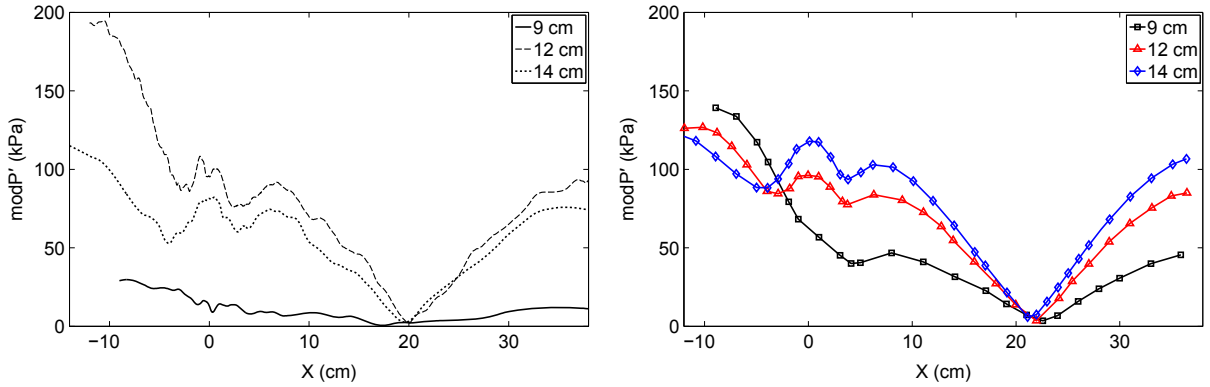

a) Present work b) Srinivasan et al. [23]

Fig. 4 First longitudinal mode shape for all three cases.

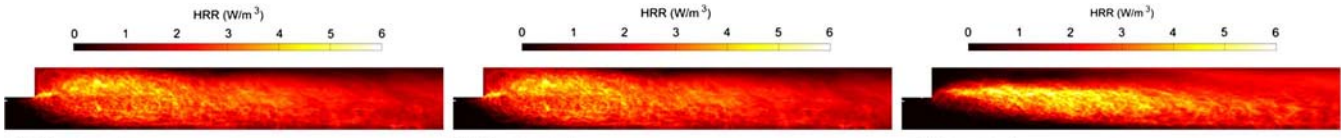

a) 14 cm post **b) 12 cm post** **c) 9 cm post**

Fig. 5 Time-averaged heat release rate for all three cases.

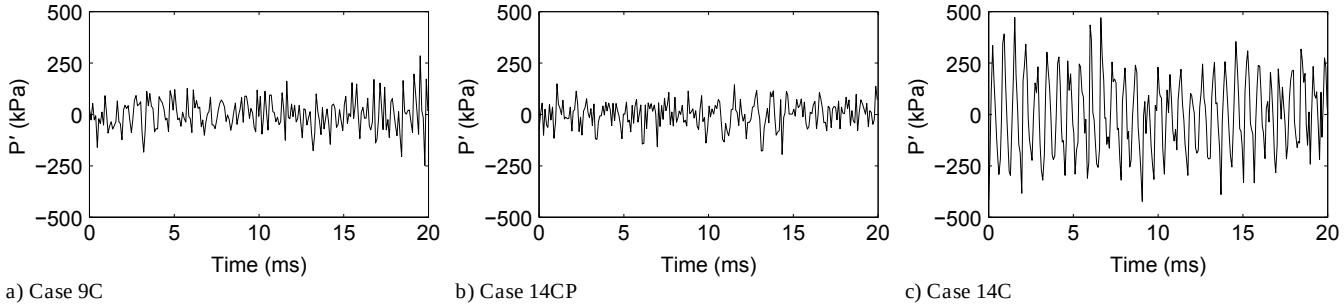

a) Case 9C b) Case 14CP c) Case 14C

Fig. 6 Pressure oscillation amplitude p' for all three cases at the dump plane in the shear layer.

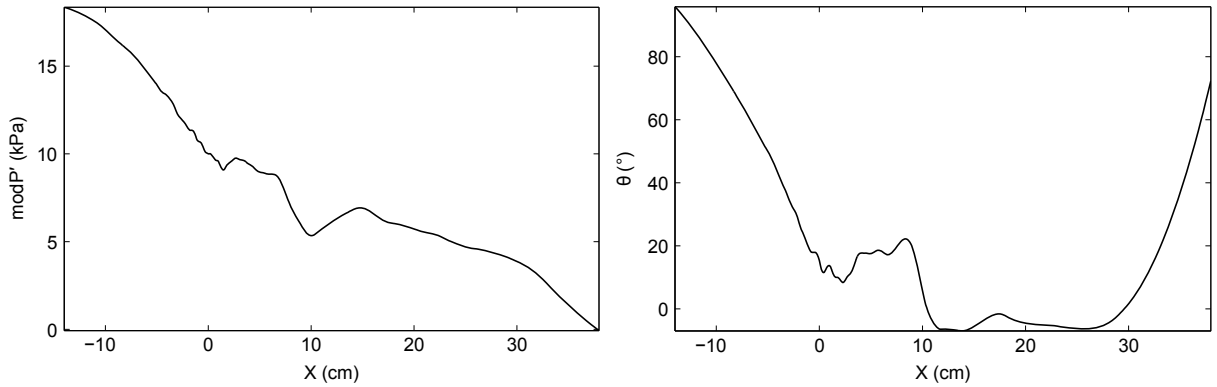

Fig. 7 First longitudinal mode shape and its corresponding phase angle for case 14CP.

branches of fuel-rich and fuel-lean premixed burning are followed by a stoichiometric diffusion burning branch, has been studied extensively for the CVRC experiments [24,52]. In our computations, triple flames are found with similar behaviors to existing computational results, as shown in the appendices for all cases. The analyses in the appendices further illustrate the flamelet/progress variable ability to correctly capture the complex flame dynamics occurring in the CVRC experiments. However, with the usage of relatively coarse meshes, we cannot present the triple flame as a conclusive analysis with complete confidence.

1. *Baroclinic Torque*

The next mechanism being studied is the baroclinic torque. The vorticity equation for a general 3-D flow is written as follows:

$$\frac{\partial \omega_i}{\partial t} + u_j \frac{\partial \omega_i}{\partial x_j} = \underbrace{-\omega_i \frac{\partial u_j}{\partial x_j}}_{[1]} + \underbrace{\epsilon_{ijk} \frac{\partial \rho}{\partial x_j} \frac{\partial p}{\partial x_k} \frac{1}{\rho^2}}_{[2]} + \omega_j \frac{\partial u_i}{\partial x_j} + \frac{1}{Re} \frac{\partial^2 \omega_i}{\partial x_j \partial x_i} \tag{10}$$

The first term on the right-hand side of Eq. (10) is a dilational term that represents the effects of the flow expansion on the vorticity field. The second term is the baroclinic torque. The third term is called vortex tilting or stretching. This term is zero because the flow is axisymmetric. The fourth term is the vorticity diffusion term. For the high-Reynolds-number flow of interest, this term is negligible. Figure 8 shows values for three significant vorticity modifying terms left in Eq. (10) at an instance in time for case 14C.

Based on our computations, there is a monotonic increase in baroclinic torque from the stable (14CP) to the semistable case (9C) and the unstable case (14C) (not shown). The baroclinic torque, as the cross product between density and pressure gradients, will inherently increase with higher-pressure oscillations. Harvazinski et al. [24], while finding similar results to this work, concluded that baroclinic torque is an important driver in promoting instability. However, as shown in Fig. 8, the vorticity enters with the shear-layer flows at the oxidizer and fuel ports, and it is advected downstream. Vortex structures form as it flows. That is, vortex shedding occurs at the end of the splitter plate and at the backstep in the combustion chamber, and these structures are advected downstream. This is also consistent with cases 9C and 14CP, but it is not shown here for brevity. Evidently, the vorticity advection term is significantly larger than both the baroclinic torque and vorticity dilation (other researchers have not reported comparisons of various terms in the vorticity evolution equation). Therefore, baroclinic torque is not a major factor in the vorticity development, and the correlation with oscillation should not be misinterpreted. It is a result of the pressure oscillations and the density difference between fluids rather than a cause of the unstable oscillation. It is noteworthy that our conclusion is only based on axisymmetric calculations, where the effect of vortex–strain interactions such as vortex stretching–tilting are not present. Nevertheless, it should not affect our conclusion that the baroclinic torque is not a significant instability mechanism.

2. *Vortex Shedding and Flame Length*

In the following section, we will concentrate on pulse timing as the main driving mechanism in regard to the vortex and flame dynamics. Pulse timing refers to the cyclic behavior in which the pressure waves in the oxidizer post behave as a pulsing mechanism that controls the periodicity of heat release rates (HRRs).

To understand the flame and vortex dynamics, we first must understand the mean flow behaviors. Figure 9 shows the time-averaged temperature and velocity field for all three, different cases. The entire length of the chamber is shown. The top half of each subfigure corresponds to the temperature fields, whereas their bottom halves present the axial velocity field. The black isolines ($T = 2000$ K) in the temperature figures are used to identify the mean flame length. The recirculation zones are enclosed by black isolines ($U = 0$). As seen in Fig. 9, the flame as well as the recirculation zones are shorter for the unstable case (14C) as compared to the stable (14CP) and semistable (9C) cases. The mean flame lengths are 28, 26.6, and 14.6 cm for cases 9C, 14CP, and 14C, respectively. The recirculation lengths are 21.8, 20, and 6.23 cm for cases 9C, 14CP, and 14C, respectively. These differences indicate a more compact flame in case 14C as compared to cases 14CP and 9C. An explanation for these measurements can be found from the vortex-shedding frequencies. We now consider the Strouhal number, defined as [53] $St = f_v D/U$, where f_v is the vortex-shedding frequency. D is the jet flow characteristic length (taken as the oxidizer post diameter in this work), and U is the oxidizer jet axial velocity. The Strouhal number relates to the flow mixedness. The preferred mode Strouhal number, which indicates strong mixing, is between 0.1 and 0.3 [53] for dump combustor configurations such as the CVRC experimental configuration.

In case 14C, vortices are shed at a frequency of 1546.24 Hz. Case 9C has a vortex-shedding frequency of 1397 Hz. On the other hand,

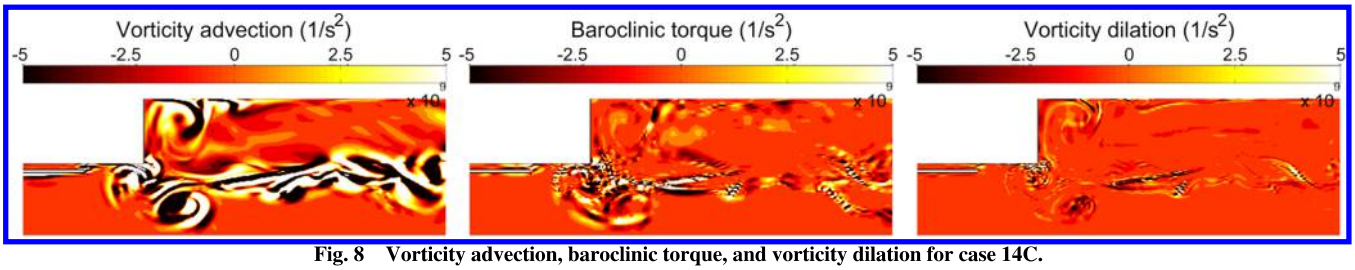

Fig. 8 Vorticity advection, baroclinic torque, and vorticity dilation for case 14C.

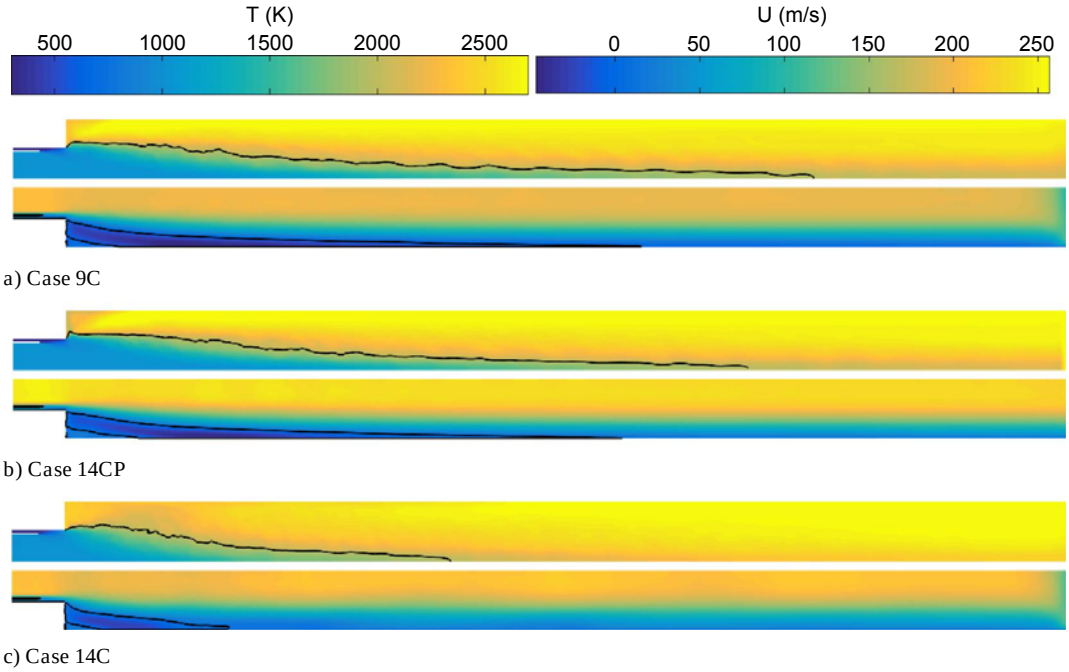

Fig. 9 Time-averaged temperature and axial velocity for all three cases.

case 14CP sheds vortices at roughly half of the frequency of its choked counterpart (800 vs 1546 Hz). Based on these frequencies, the Strouhal numbers are 0.1316, 0.1229, and 0.0878 for cases 14C, 9C, and 14CP, respectively. Therefore, the flow in 14CP is not as well mixed as in the choked cases. Furthermore, the higher the Strouhal number in the preferred range, the more likely it will form large coherent vortex structures downstream of the dump plane. This is shown to be true based on the vortex dynamics results shown in Secs. III.D.4–III.D.6.

As expected, due to lack of transport across the centerline, our axisymmetric simulations predict longer flames than 3-D calculations. As shown in Fig. 9, comparing case 14CP to case 14C, the flame becomes more compact as the flow becomes more unstable, as is also evident by the Strouhal numbers. Therefore, comparing with previous axisymmetric results from Garby et al. [29], it appears that larger-pressure oscillation amplitudes in our simulations contribute to increased mixing, and thus shorter flames. Moreover, Sardeshmukh et al. [33] showed that simulations with detailed chemistry mechanisms predicted much higher-pressure oscillations as compared to ones with global chemistry mechanisms. The difference in chemical mechanisms can thus also affect the differences in flame lengths. However, without rigorous comparisons between different results, these explanations remain unverified.

3. *Energy Release Rate*

To understand the interaction between acoustic and flame behaviors, the Rayleigh index will be used as a guideline in the following section. The Rayleigh index is a correlation used to determine the locations where the pressure oscillations are being driven or damped by the unsteady heat release rate. The time-averaged spatially local Rayleigh index (RI) [29] is defined as

$$RI = \frac{1}{\tau}\int_{t_o}^{t_o+\tau} \frac{\gamma-1}{\gamma} p'\dot{\omega}' \, \mathrm{d}t$$

where p' is the local pressure oscillation, and $\dot{\omega}'$ is the local HRR oscillation. A positive Rayleigh index indicates the pressure oscillations are driven by the unsteady HRR. Figure 10 presents the Rayleigh index results for all three cases. Only half of the combustion chamber is shown in these plots.

Figure 10 shows a strong correlation between the pressure oscillations and the HRR around the recirculation zone for the 14C case, as well as the mixing layer immediately after the splitter plate. In case 14CP, a large damping region is observed immediately after the backstep. In the shear layer of the combustion chamber, small instability-driven regions are found along with damping regions. Case 9C exhibits a behavior that is a combination of both cases 14C and 14CP. A large instability-driven region is found along the shear layers in the combustion chamber. This region is surrounded by smaller damping regions near the recirculation zone and the centerline. It is noted that the maximum values of the Rayleigh index in cases 9C and 14CP are an order of magnitude smaller than case 14C. This means the unsteady HRR drives the instability more strongly in case 14C as compared to case 9C.

Based on the flame length calculated and the Rayleigh index analysis, the following analyses will be performed for all three cases, focusing on the region enclosed by the dump plane ($x = 0$) and the mean flame length of case 14C ($x = 15$ cm), as shown by the two vertical broken lines in Fig. 10c. This region will now be called volume 1.

4. *Mechanisms for Combustion Instability in Case 14C*

Figure 11a shows the volume-averaged HRR and pressure of volume 1 for case 14C. The volume-averaged method is used to remove any phase-lag bias due to the spatial locality of the pressure signal in volume 1. As seen in Fig. 11a, the HRR is completely in phase with the pressure oscillation, further confirming our Rayleigh index analysis. Figure 11b shows the pressure signal for approximately two cycles. There are five circle markers on the plot, identifying the five time instances analyzed in the following discussion. These time instances are referred to as t1 to t5.

Because the dominant pressure waves are longitudinal, the transverse pressure gradients are found to be negligible. Therefore, the pressure field will be best represented as axial functions. Figure 12 shows the pressure signal along the centerline at different instances in time marked by the previously described circles in Fig. 11b. The dump plane is located at $x = 0$ cm.

Figure 13 shows contour plots of the vorticity, HRR, fuel, and oxidizer mass fractions for a complete cycle from times t1 to t5 for case 14C. Time is different for each row of subfigures. These time instances from top to bottom correspond to the circles in Fig. 11b from left to right. The fuel mass fraction contour plots are drawn on a different color map as compared to the other three quantities. The domain shown is from $x = -1.5$ cm to $x = 10$ cm.

The cycle begins at time t1, corresponding to the first pressure peak noted by the first circle in Fig. 11b. As seen in Fig. 13, most of the

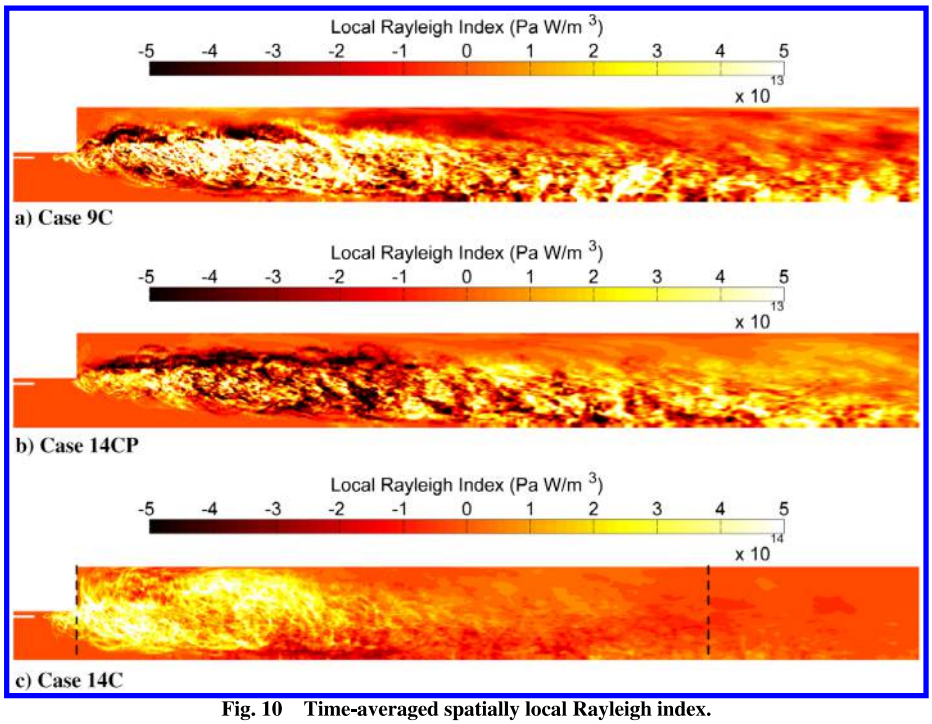

Fig. 10 Time-averaged spatially local Rayleigh index.

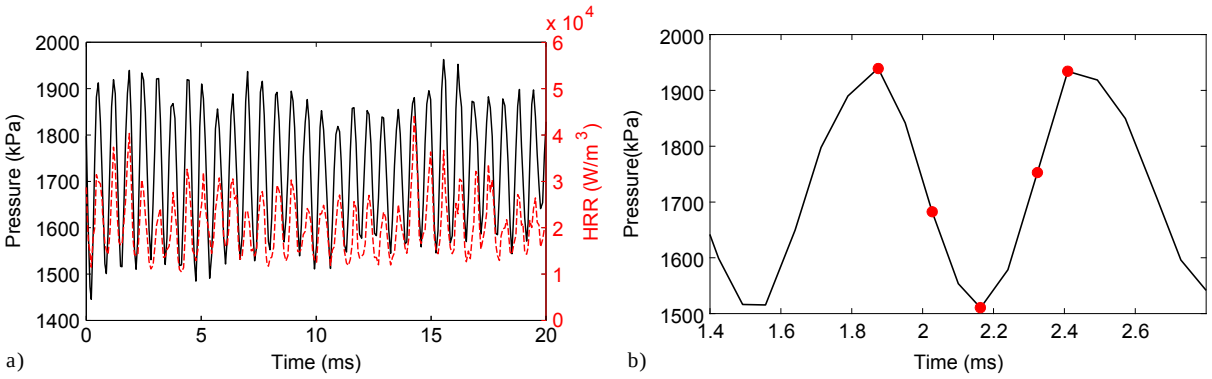

Fig. 11 Volume-averaged heat release rate and pressure of volume 1 for case 14C.

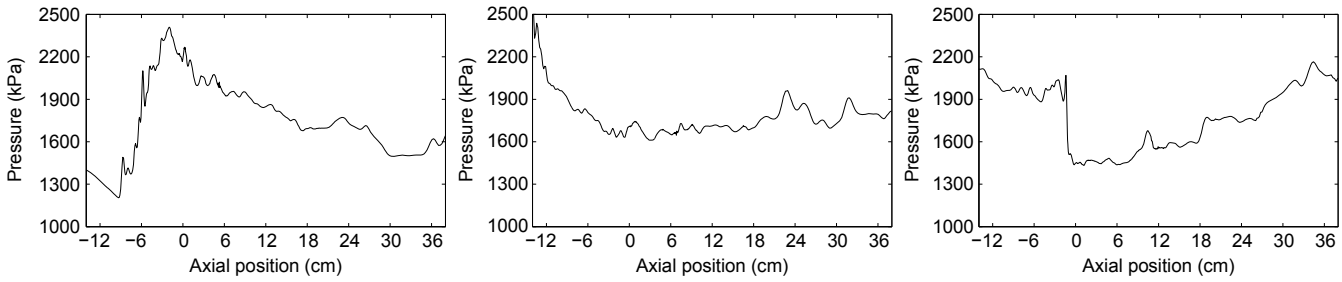

a) Pressure at t1 b) Pressure at t2 c) Pressure at t3

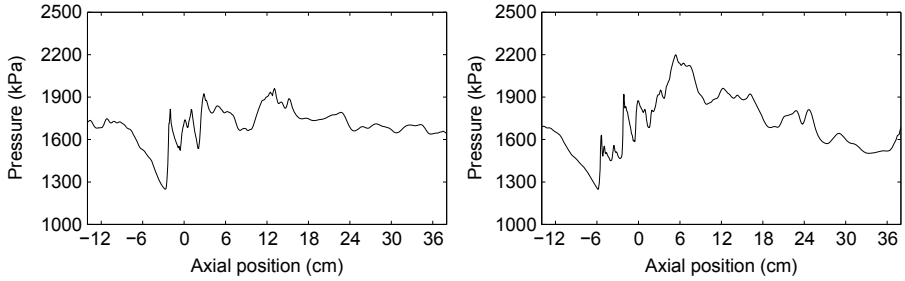

d) Pressure at t4 e) Pressure at t5

Fig. 12 Spatial pressure variation for the entire computational domain for 14C.

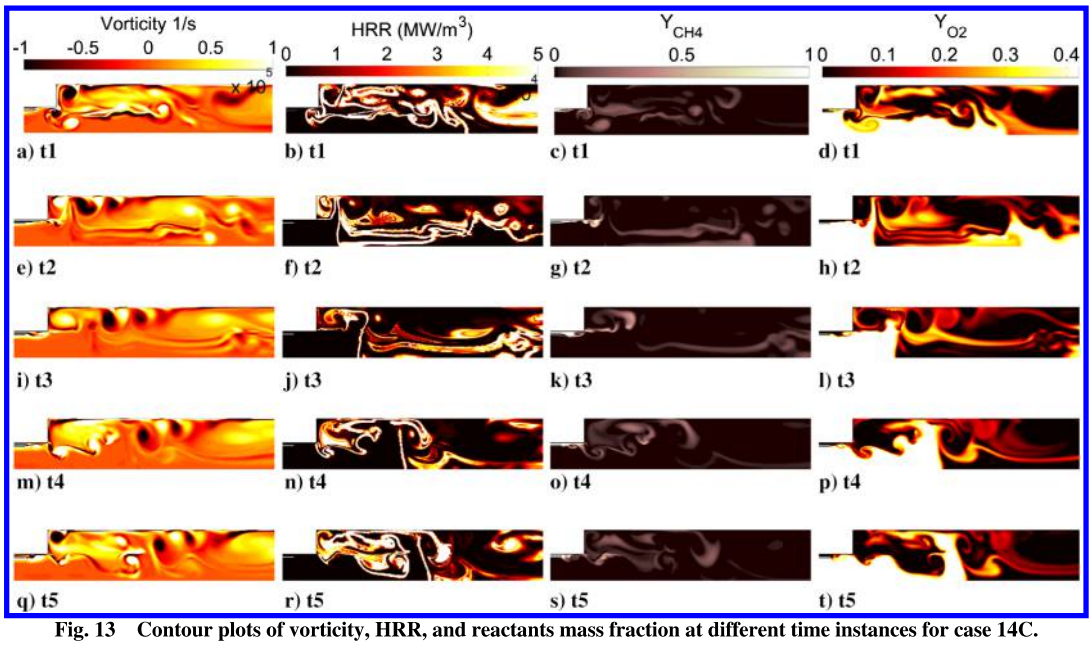

Fig. 13 Contour plots of vorticity, HRR, and reactants mass fraction at different time instances for case 14C.

reactions happen in the two largest vortex structures: one immediately after the dump plane and one further downstream around $x = 0.01$ m. At this instance, the pressure peaks around the dump plane. These vortex structures enhance turbulent mixing and allow premixed burning to occur inside of these structures while non-premixed burning surrounds them (not shown). In the meantime, there are small vortices shed along the shear layer after the dump plane, and they carry with them unburned fuel toward the unburned oxygen stream along the centerline, as seen in Figs. 13a and 13c. As shown in Figs. 12a–12c, a pressure wave traveling downstream from the dump plane ($x = 0$ cm) toward the combustion chamber exit at t3 and pressure waves traveling upstream toward both the inlets of the reactants at t1 are observed. The pressure waves traveling upstream impose an adverse pressure gradient on the reactant streams, causing a disruption of the reactant flow into the combustion chamber. At this instance of time, the adverse pressure gradient is even strong enough to push a mixture of fuel and oxidizer from the splitter plate region into the fuel post, as shown in Figs. 13c and 13d.

At time t2, because of the favorable pressure gradient in the combustion chamber from time t1 (Fig. 12a), the large vortex structures in the recirculation zone are advected further downstream. The previously unburned reactants along the centerline from time t1 are now ignited, as shown in Fig. 13f. Now, the upstream traveling pressure waves are now reflected from both the inlets, as shown in Fig. 12b, and they create a favorable pressure gradient that pushes these reactant streams into the combustion chamber. An expanded oxidizer impinging jet is found in all the subsequent time instances because of the reflected downstream running wave at this time instance. Similarly, a large fuel concentration is found around the dump plane due to the favorable pressure gradient.

At time t3, the downstream traveling pressure wave in the oxidizer post is now approaching the splitter plate ($x = -10$ cm), as seen from Fig. 12c. The favorable pressure gradient in the oxidizer post now accelerates the flow, pushing the accumulated reactants from the mixing layer into the recirculation zone. Meanwhile, an adverse pressure gradient is found in the same recirculation region. This adverse pressure gradient prevents the newly shed vortex structures, which carry the reactants, from moving farther downstream.

At time t4, vortex structures shed from the mixing layer continue to merge and form a large coherent structure in the recirculation zone. Due to the formation of the large coherent structure, the reactants are allowed sufficient time to be mixed as well as heated by the hot product gases present in this zone. The increase in reaction rate at time t4 causes a rise in chamber pressure, specifically in the region from the dump plane to $x = 8$ cm. Now, the reflected pressure wave from the chamber exit is approaching the same region, with its peak found at $x = 12$ cm, as seen from Fig. 12d. This phenomenon creates a syncing/coupling mechanism between the pressure and the HRR, thus further promoting combustion instability.

At time t5, the mixture in the recirculation zone finally combusts, creating large separated pressure waves traveling upstream of the reactant posts as well as downstream of the combustion chamber. The cycle is now poised to repeat itself. It is noteworthy that the adverse pressure gradient imposed by the upstream traveling waves is not as large the one found at t1, as shown in Fig. 12e. This means the mixture found at the splitter plate cannot travel upstream of the fuel post, as shown in Figs. 13s–13t.

5. *Mechanism for Combustion Instability in Case 9C*

Figure 14a shows the volume-averaged HRR and pressure of volume 1 for case 9C. The HRR in this case is intermittently in phase with the pressure oscillations, further confirming its semistable classification in which the oscillation amplitudes never reach a limit-cycle behavior. Therefore, the following analysis is not truly a cycle analysis but, nevertheless, a description of the oscillatory behavior in this case. The circles in Fig. 14b denote the five time instances described by Fig. 16

Similar to case 14C, the pressure field in the computational domain is presented as a one-dimensional function in the axial direction, as shown in Fig. 15

Figure 16 shows the contour plots of the vorticity, HRR, fuel, and oxygen mass fractions at various time instances. The fuel mass fraction contours are again drawn on a different color map as compared to the other three quantities. The domain shown in these plots is the same as in Fig. 13

The first distinctive feature in case 9C as compared to case 14C is the lack of vortex merging phenomena occurring immediately downstream of the backstep. Instead, smaller vortex structures are shed and advected downstream immediately. The vortex merging occurs further downstream from the dump plane, creating a lumped reaction zone similar to the one found in the recirculation zone in case 14C. A long, thin reaction zone is found within the shear layer immediately downstream of the backstep. Comparing the pressure contour plots between times t1 and t2 in Fig. 16, there is clearly (again) a left-running pressure wave propagating toward the oxidizer inlet. However, these pressure gradients are not strong enough to cause a disruption in reactants flow as compared to case 14C. Instead, these pressure gradients simply push the fuel against the horizontal wall before the backstep, temporarily hindering the reactants mixing. Stronger premixed burning is found in the recirculation zone at the peak of the pressure oscillation as compared to its trough (not shown).

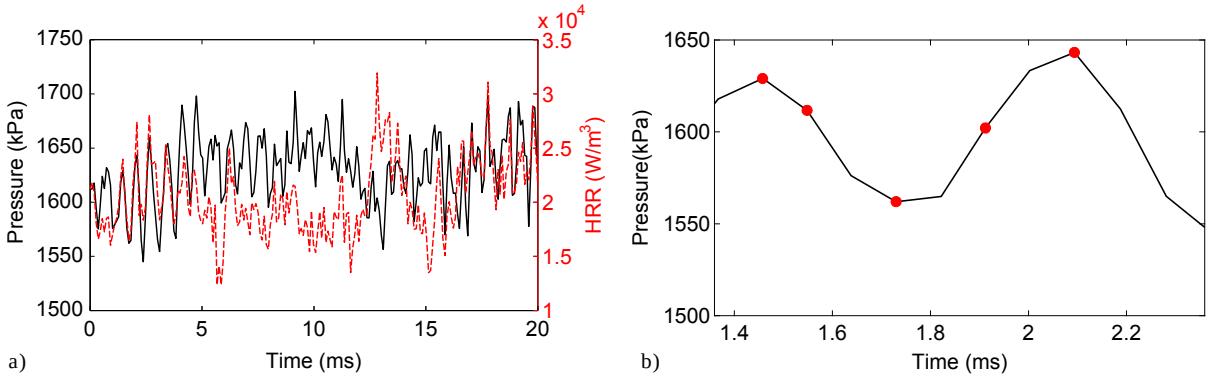

Fig. 14 Volume-averaged HRR and pressure of volume 1 for case 9C.

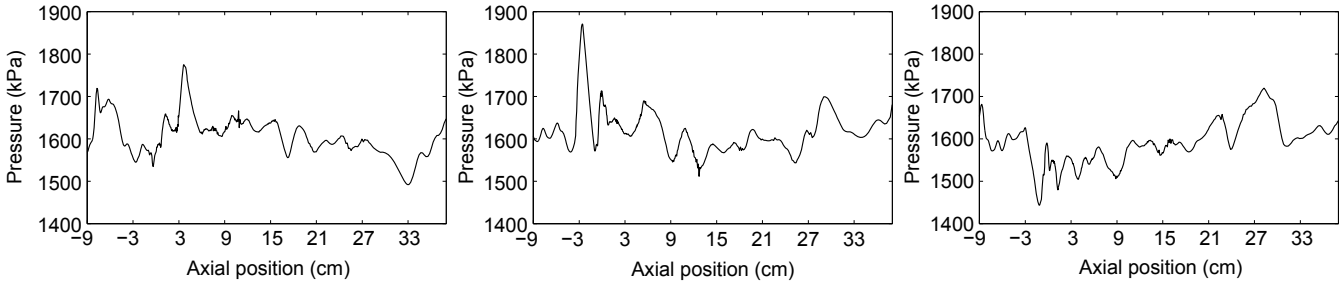

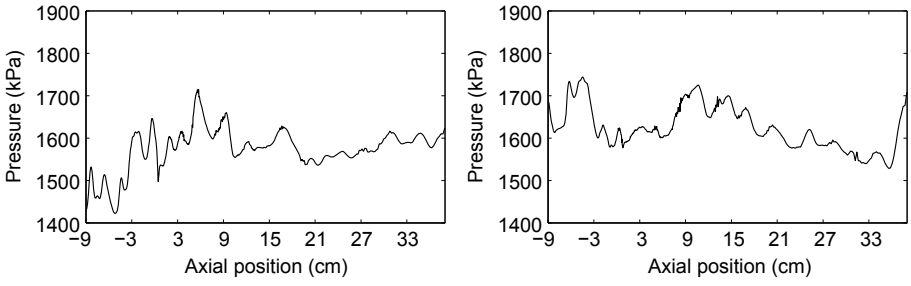

Fig. 15 Spatial pressure variation for the entire computational domain for case 9C.

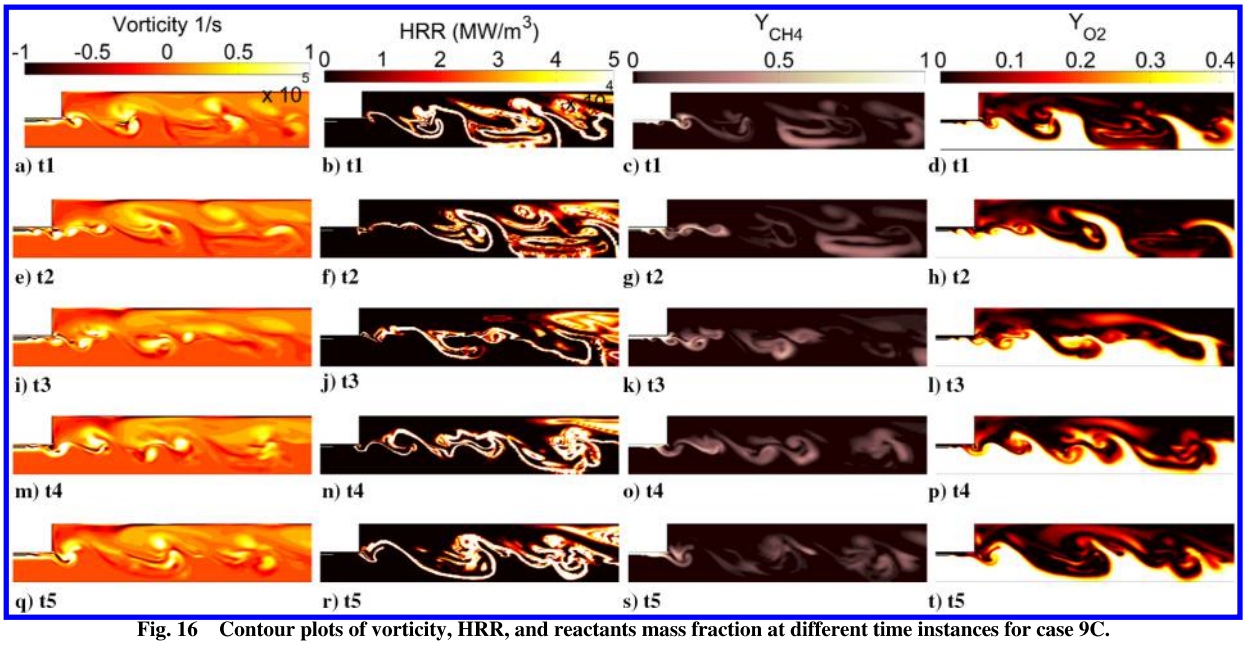

Fig. 16 Contour plots of vorticity, HRR, and reactants mass fraction at different time instances for case 9C.

6. *Mechanism for Combustion Instability in Case 14CP*

Figure 17a shows the volume-averaged heat release rate and pressure of volume 1 for case 14CP. The HRR in this case is completely out of phase with the pressure oscillations. The circles in Fig. 17b denote the four time instances described by Fig. 19.

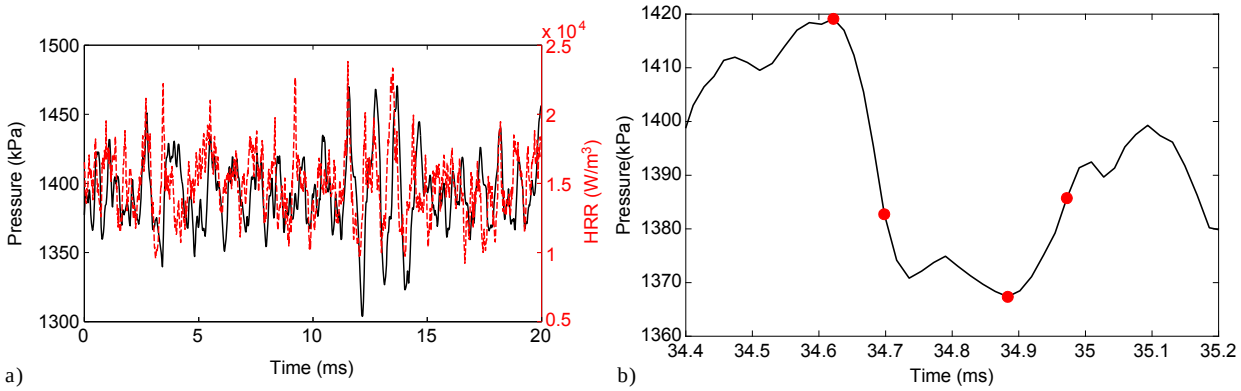

a) b)

Fig. 17 Volume-averaged heat release rate and pressure of volume 1 for case 14CP.

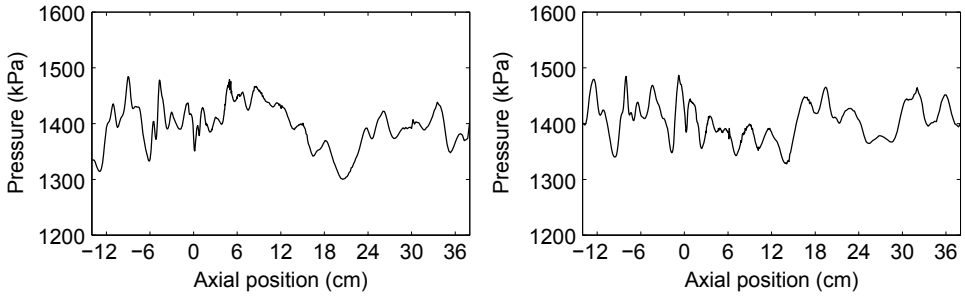

a) Pressure at t1 b) Pressure at t2

c) Pressure at t3 d) Pressure at t4

Fig. 18 Spatial pressure variation for the entire computational domain for case 14CP.

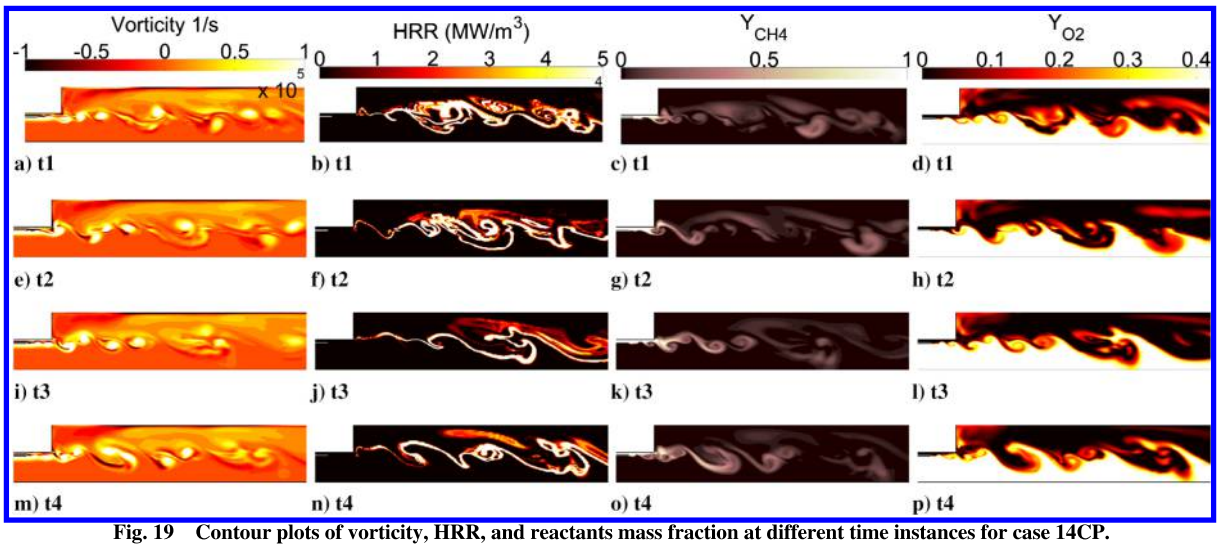

Fig. 19 Contour plots of vorticity, HRR, and reactants mass fraction at different time instances for case 14CP.

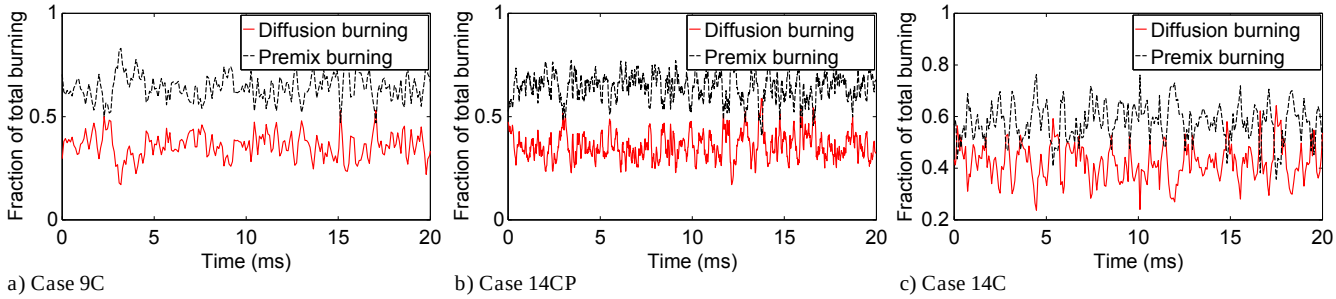

a) Case 9C b) Case 14CP c) Case 14C

Fig. 20 Burning modes of volume 1 as functions of time.

Figure 18 shows the pressure field in the computational domain as a one-dimensional axial function. Each of the subfigures corresponds to different instances in time marked by the circles in Fig. 17b.

Figure 19 shows contour plots of the vorticity, HRR, fuel, and oxygen mass fractions at various time instances on the same domain as Figs. 16 and 13.

In this case, there is no distinctive vortex merging pattern. Therefore, the lumped reaction zones present in case 14C and, to a degree, in case 9C are not found in this case. Instead, the vortex structures shed in the shear layer immediately after the backstep are simply advected downstream. These vortex structures simply carry the reactants downstream until sufficient mixing is achieved and the mixture combusts. Therefore, most of the reactions can be found within the shear layer.

7. *Premixed Versus Diffusion Flame*

To further assess the FPV capability of predicting partially premixed flames, the flame index (FI) is used [23]. It has the following form:

$$\mathrm{FI} = \frac{\nabla Y_f \cdot \nabla Y_o}{|\nabla Y_f||\nabla Y_o|}|\dot{\omega}_f| \tag{11}$$

where FI is negative for diffusion and positive for the premix burning mode. The first factor on the right side of Eq. (11) is the classic Takeno index. Its value is $+1$ when the reactant gradients are on the same side (premix) and -1 when the fuel and oxidizer are on opposite sides of each other (non-premixed). The second factor on the right is the volumetric fuel reaction rate $\dot{\omega}_f$. Therefore, the flame index, as a product of these two terms, represents burning mixtures in either a premixed or non-premixed mode.

Figure 20 shows the results for fuel consumption rates of different burning modes as fractions of the total fuel consumption in volume 1. The results are obtained by separately integrating the negative and positive values of the flame index, which are normalized by the total volume integral of the fuel consumption rate.

In all three cases, the premixed burning mode accounts for roughly 60% of the total HRR. However, as seen in Fig. 20, the dominant mode switches between non-premixed and premixed for all three cases. The mode switching happens more consistently in the unstable case as compared to the 14CP and 9C cases. These findings are consistent with the results by Srinivasan et al. [23]. However, in the unstable cases, more frequent mode switches occur in their computations.

IV. Conclusions

A code for compressible axisymmetric chemically reacting flow in a rocket combustion chamber is developed. Pressure results are benchmarked against both existing experimental and computational results. The semistable case 9C matches experimental results very well. In the unstable cases, all existing computations including the current work underpredict the pressure oscillation magnitude while overpredicting the oscillation frequency. Existing 3-D computations predict oscillation amplitudes within 90% of the experimental data. Existing axisymmetric calculations using global chemical mechanism results are within 50–60% of the experimental data. In the current work, the pressure oscillation amplitudes are within 80–85% of the experimental data. All simulations including the current work overpredict the oscillation frequencies because of the adiabatic wall boundary condition. On the other hand, the current simulation times are at least 50 times less expensive than existing axisymmetric calculations. Spatial mode decomposition in the first harmonic based on the PSD analysis matches existing 3-D results very well for the unstable cases. There are half-wave acoustical standing waves found in the combustion chamber.

An additional simulation is performed using an open-end exit boundary condition for the 14 cm oxidizer post length. Comparisons are made with a semistable case (9C) and completely unstable case (14C). Time-averaged flowfields reveal longer flame lengths for the unstable case as compared to 3-D simulations but more compact flame as compared to existing axisymmetric simulations. The flame becomes longer as the flows transition from unstable to stable behavior. In the choked cases, the vortex-shedding frequency is found to be within the Strouhal preferred mode frequency, leading to higher flow mixedness as compared to the stable (open-end) case.

In the 14 and 12 cm oxidizer post with a choked nozzle, Rayleigh index analyses reveal strong correlations between the pressure fluctuations and the heat release rate around the upstream pressure antinode in the chamber, causing a destabilizing effect in the chamber. In the semistable and stable cases, strong correlations between the pressure oscillations and heat release rates can only be found around mixing shear layers.

Cycle-to-cycle analyses further confirm the Rayleigh index findings. In case 14C, highly intense (lumped) reaction zones are found near the dump plane (pressure antinode). In case 9C, these lumped reaction zones move further away from the dump plane and closer to the pressure node. This phenomenon has a stabilizing effect on the combustion chamber. In case 14CP, no lumped reaction zones are found.

The behaviors described using the aforementioned analyses are all consistent with various computational findings from different groups, further validating the newly developed code.

In the existing literature, there are only two simulations with detailed chemical mechanisms [31,33]. The production of secondary radicals such as CO+ and OH−, however, is not reported. Therefore, further investigation into the current code capability to compute such radicals and their roles in the combustion process should be valuable. The importance of radical advection is diminished when those species concentrations are largely determined through partial equilibrium and steady-state balances. Implicitly, there is reliance on those balances in using the flamelet model here.

Appendix A: Numerical Implementation

All the transport equations including the main flow [Eqs. (1–3)], turbulence models [Eqs. (4) and (5)], and flamelet [Eqs. (7–9)] are solved simultaneously using the same numerical scheme as described previously. The following scheme can be found in references [42,43] and it is described here for completeness. For simplicity, the numerical details presented in the section are in one-dimensional form. Extension to either two or three dimensions is straightforward.

Take a generalized fully conservative equation in one-dimensional form:

$$\frac{\partial W}{\partial t} + \frac{\partial F}{\partial x} = \frac{\partial G}{\partial x} + \frac{\partial d}{\partial x} \tag{A1}$$

where W is a conserved variable such as density ($\bar{\rho}$), axial ($\bar{\rho}\ \tilde{u}$), or radial ($\bar{\rho}\ \tilde{v}$) momentum; F represents the inviscid mass flux; and G represents the diffusion mass flux. Note that d is the artificial dissipation term in the following form:

$$d_{j+1/2} = d^{(2)}_{j+1/2} + d^{(4)}_{j+1/2} \tag{A2}$$

where the superscripts (2) and (4) represent their respective order (second and fourth). The second-order dissipation term has the following form:

$$d^{(2)}_{j+1/2} = \epsilon^{(2)}_{j+1/2}\lambda_{j+1/2}(W_{j+1} - W_j) \tag{A3}$$

where $\lambda_{j+1/2}$ is the maximum one-dimensional wave speed:

$$\lambda_{j+1/2} = \max(|u_j| + a_j, |u_{j+1}| + a_{j+1}) \tag{A4}$$

and u is the flow velocity and a is acoustical wave speed.

Similarly, the fourth-order dissipation term has the following form:

$$d^{(4)}_{j+1/2} = -\epsilon^{(4)}_{j+1/2}\lambda_{j+1/2}(U_{j+2} - 3W_{j+1} + 3W_j - U_{j-1}) \tag{A5}$$

The second- and fourth-order switching functions have the following forms:

$$\epsilon^{(2)}_{j+1/2} = \kappa^{(2)} \max(\nu_{j-1}, \nu_j, \nu_{j+1}, \nu_{j+2}) \tag{A6}$$

and

$$\epsilon^{(4)}_{j+1/2} = \max[0, \kappa^{(4)} - \epsilon^2_{j+1/2}] \tag{A7}$$

where the coefficients $\kappa^{(4)}$ and $\kappa^{(2)}$ are taken as $1/32$ and $1/2$, respectively. The pressure sensor has the following form:

$$\nu_j = \frac{|p_{j-1} - 2p_j + p_{j+1}|}{|p_{j-1} + 2p_j + p_{j+1}|} \tag{A8}$$

In the time-integration scheme, the diffusive flux is only evaluated one time at the beginning of the time step. This technique is proven to save computational costs while maintaining the overall order of accuracy of the scheme [42]. The time-integration scheme is described as follows:

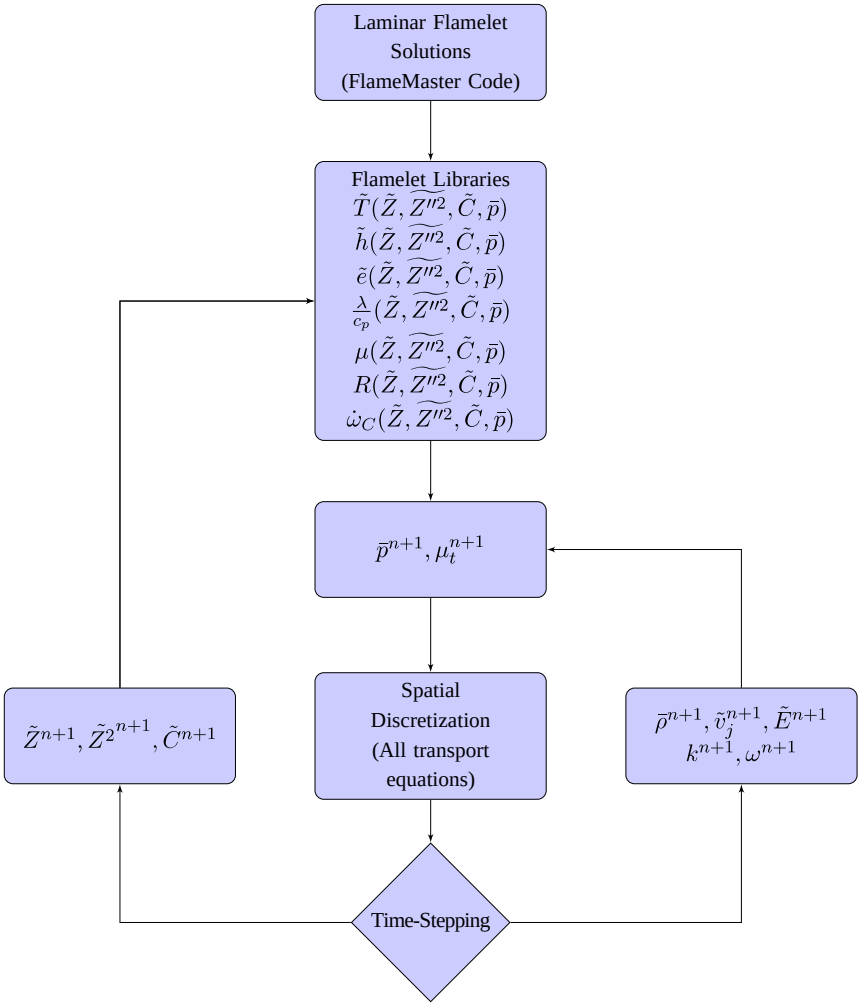

Fig. A1 Overall solution procedure of the developed code.

$$
\begin{aligned}
W^{(1)} &= W^{(n)} \\
W^{(2)} &= W^{(n)} + \frac{\Delta t}{4}\left[-\frac{\partial F}{\partial x}^{(1)} + \frac{\partial G}{\partial x}^{(1)}\right] \\
W^{(3)} &= W^{(n)} + \frac{\Delta t}{3}\left[-\frac{\partial F}{\partial x}^{(2)} + \frac{\partial G}{\partial x}^{(1)}\right] \\
W^{(4)} &= W^{(n)} + \frac{\Delta t}{2}\left[-\frac{\partial F}{\partial x}^{(3)} + \frac{\partial G}{\partial x}^{(1)}\right] \\
W^{(n+1)} &= W^{(n)} + \Delta t\left[-\frac{\partial F}{\partial x}^{(4)} + \frac{\partial G}{\partial x}^{(1)}\right] \\
W^{(n+1)} &= W^{(n+1)} + \Delta_t \frac{\partial d}{\partial x}^{(n+1)}
\end{aligned} \tag{A9}
$$

A flowchart of the overall code is also given for further reference in Fig. A1.

Appendix B: Triple Flames

To correctly capture the triple flame, the combustion model should first be able to simulate partially premixed flames. The following paragraphs will further illustrate the current FPV model capability.

Figure B1a shows the maximum flame temperature as a function of the stoichiometric scalar dissipation rate χ_{st}. This S-shaped curve is very useful in demonstrating the nature of flamelets. The upper branch describes stable burning solutions (circle marker). The lower branch (horizontal line with the diamond marker) describes nonburning solutions. The middle branch (black line with the diamond marker) shows the unstable burning solutions. In the traditional diffusion flamelets approach proposed by Peters [38], the laminar flamelet solutions are parameterized by the mixture fraction and the scalar dissipation rates. However, as seen in Fig. B1a, there are multiple flame temperatures for a single value of χ_{st}. So, for the traditional diffusion flamelet approach, only the upper part of the branch can be described, thus limiting it to only full diffusion burning solutions.

Figure B1b shows the progress variable as a function of the stoichiometric scalar dissipation rate. Similar to Fig. B1a, multiple progress variable values are found for a single value of χ_{st}. However, one-to-one mapping exists between the flame temperature and the progress variable, as shown in Fig. B1c. Therefore, by parameterizing the flamelet solutions by the progress variable, the full flamelet solution space can be accessed, and the local flame extinction and reignition can be fully described. These solutions now include the partially premixed flame case.

Figure B2 shows the flamelet solutions at different values of the progress variable. The solid curves without any marker describe the progress variable reaction rate as functions of the mixture fraction. The curves with different marker types represent species mass fractions as functions of the mixture fraction. Figure B2a represents an unstable burning solution ($Y_C = 0.05$), in which the reactants are not completely consumed, which allows for a high probability of premixing. This represents a situation with the CVRC configuration in which the flow is dominated by the mean strain rate, especially upstream of the dump plane in the mixing shear layer. Figure B2b represents a complete diffusion flame solution, because most of the reactants are consumed. This represents most of the situation further downstream of the dump plane, which is prominently featured outside of the recirculation zone.

Because of the FPV approach ability to describe the full flamelet solution space, which allows for incomplete reactions with partial mixing, the model can describe both premixed and non-premixed

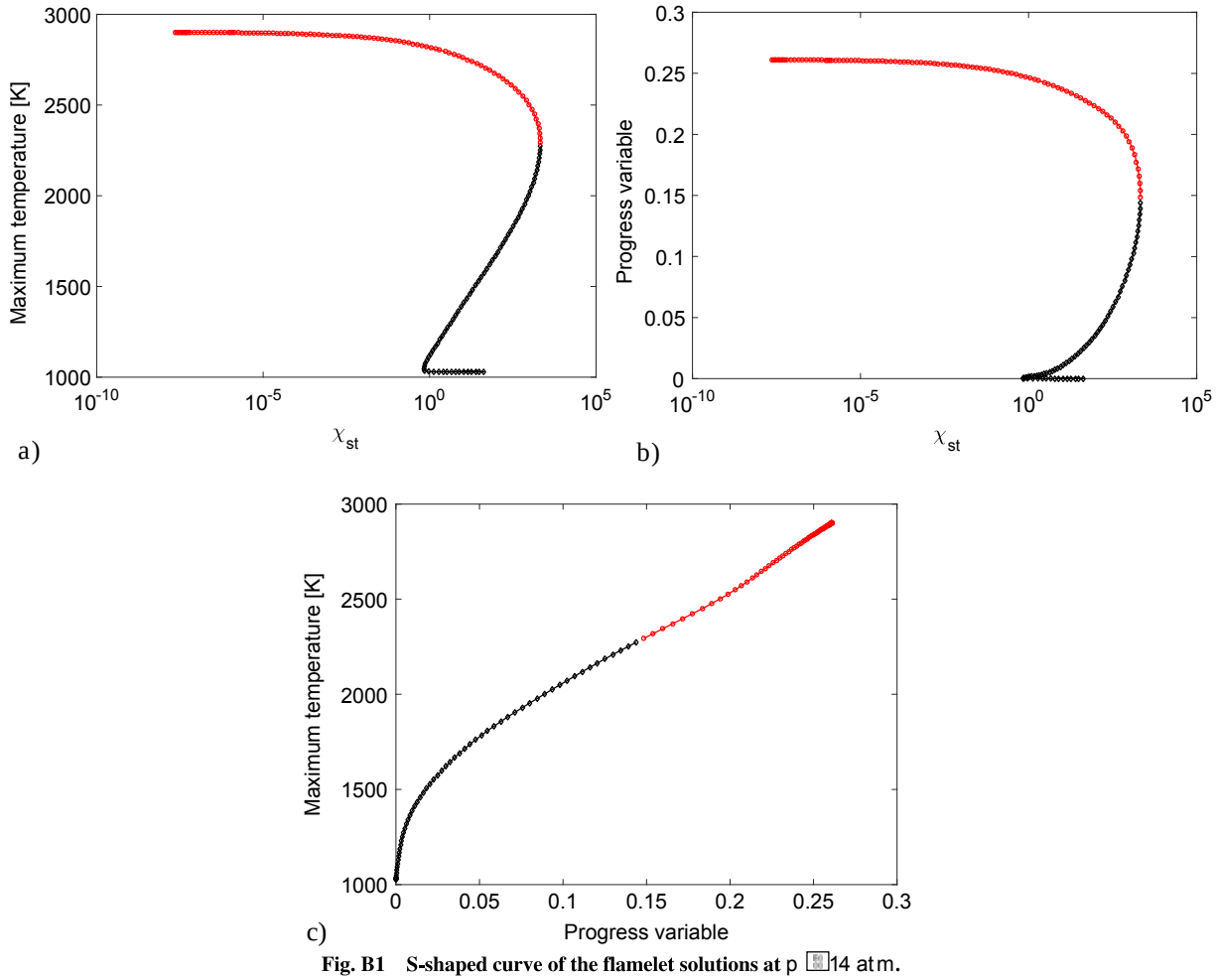

Fig. B1 S-shaped curve of the flamelet solutions at p 14 atm.

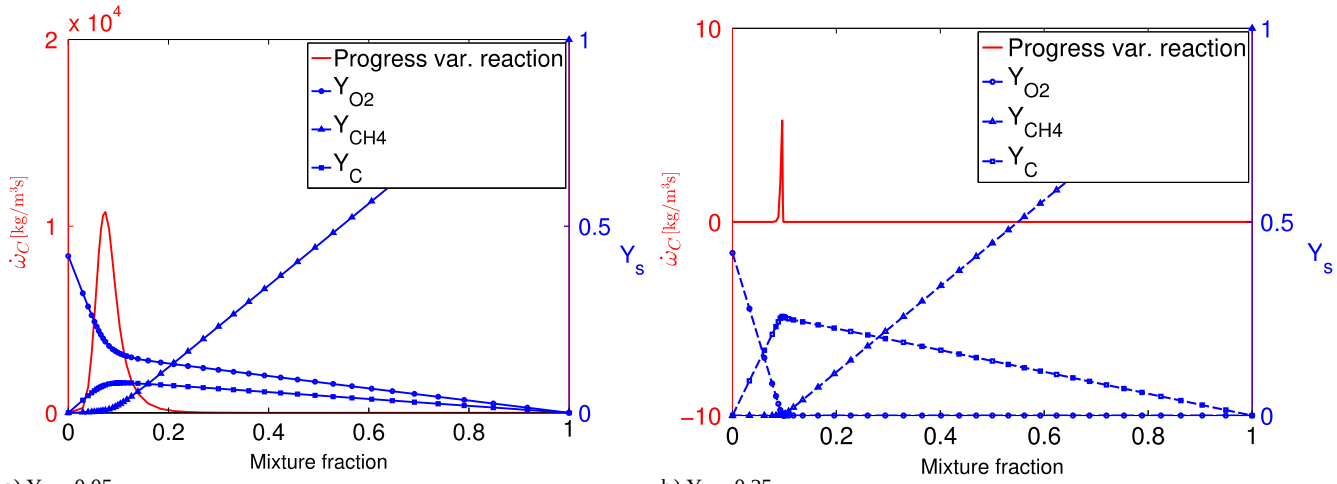

Fig. B2 Flamelet solutions at different values of the progress variable (Prog. var.) for p = 14 atm.

burning modes simultaneously. The flames in these situations are called partially premixed flames. This is different than fully premixed flames, where the model is required to capture a clear turbulent flame speed. The FPV approach has been successfully applied to partially premixed flames [39,54,55].

As shown in Sec. III.D.7, there is a partially premixed flame present in the combustion chamber. Srinivasan et al. [23] and Harzavinski et al. [24] further showed the presence of multiple triple flame points in the combustion chamber. The following sections show our code's capability to capture these points and further discusses why this analysis is not included in the main paper's body.

Figure B3 shows the HRR for the 14C case at four different times. These time snapshots are at the same time interval shown in Fig. 13. However, they are zoomed-in near the dump plane. There are two different isocontours superimposed on these plots. The lighter isocontours represent the locations of the stoichiometric mixture fraction. The darker isocontours represent the mean flame temperature ($T = 2000$ K). The intersections between these isocontours that lie in the reaction zone represents triple flame points, as marked by the circles.

At the top of the cycle, or time t1, the flame is strongly anchored at the backstep, with multiple triple flame points surrounding the corner of the dump plane. At time t2, after the pressure waves move away from the dump plane, the number of the triple flame points not only decreases but the most upstream triple flame point now moves further downstream of the dump plane. At time t3, or the lowest-pressure point, the triple flame's points are the furthest away from the dump plane. Additionally, the flame is weakly anchor/detached from the

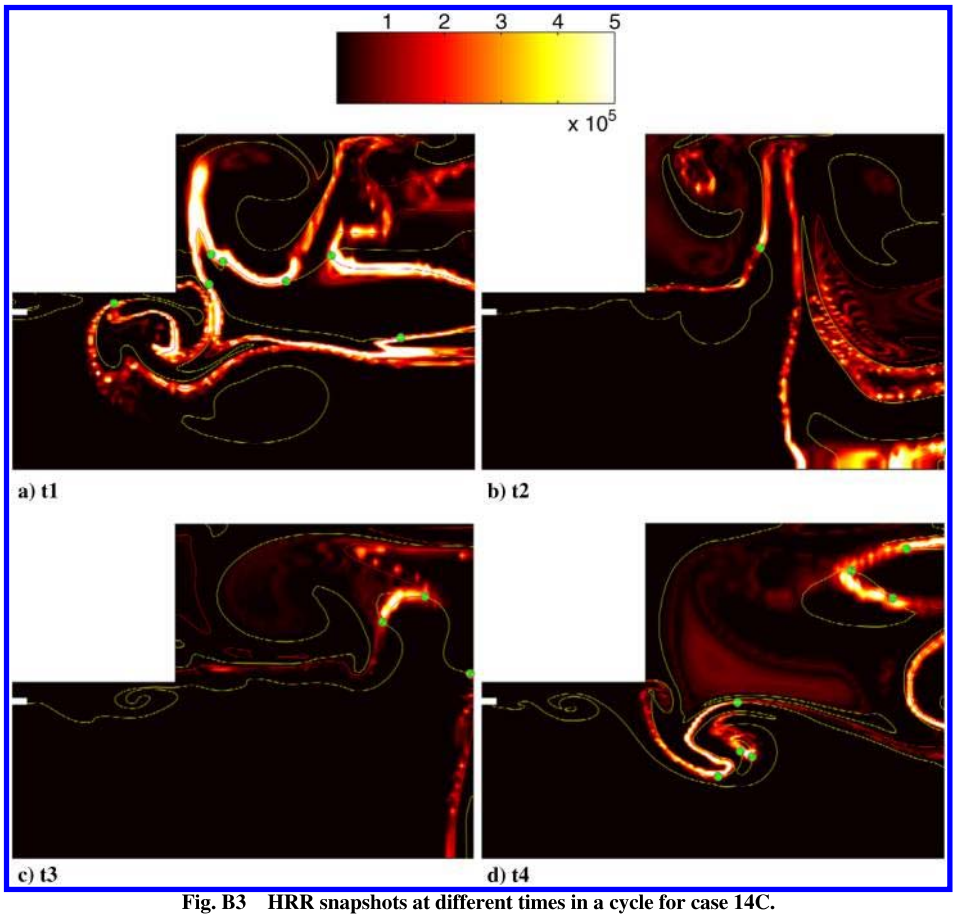

Fig. B3 HRR snapshots at different times in a cycle for case 14C.

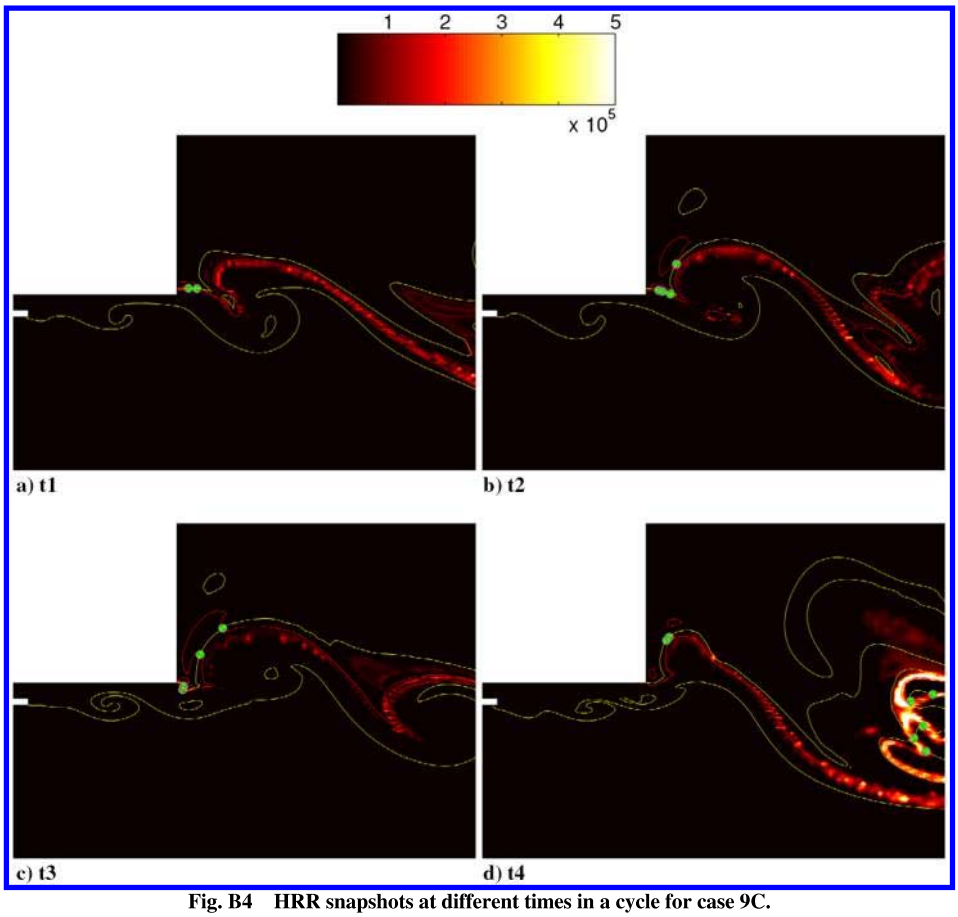

Fig. B4 HRR snapshots at different times in a cycle for case 9C.

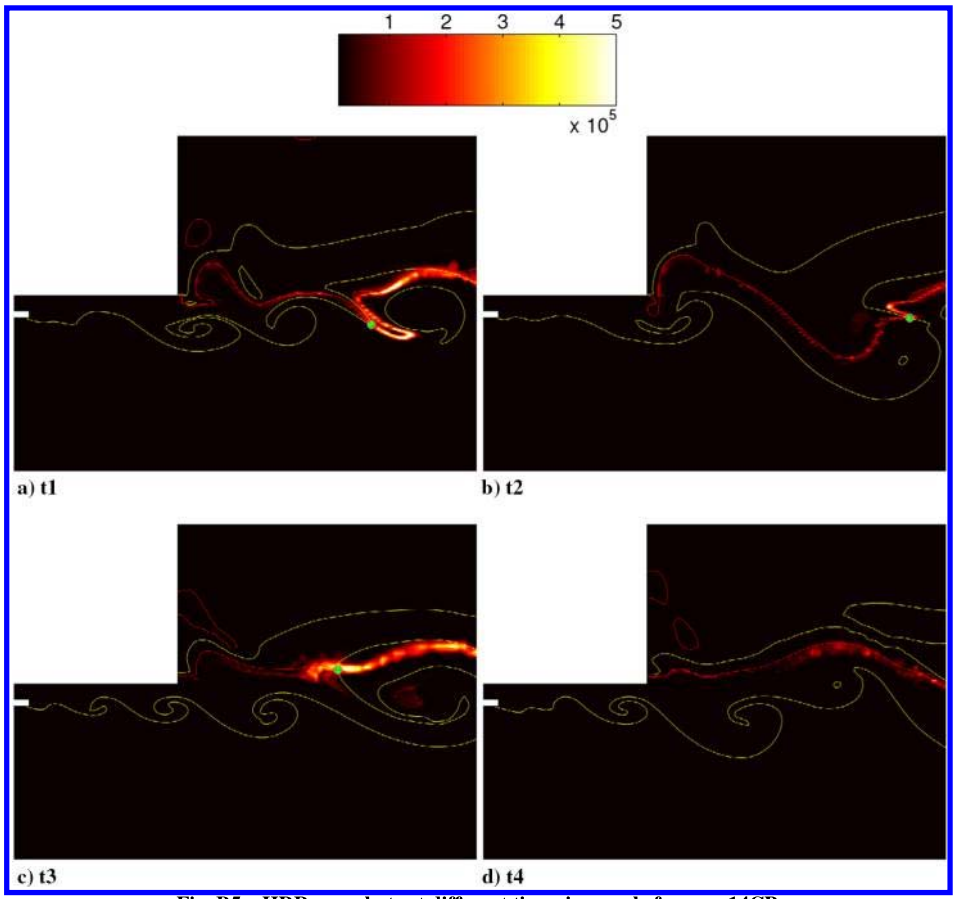

Fig. B5 HRR snapshots at different times in a cycle for case 14CP.

backstep. At time t4, as the traveling wave in the chamber is reflected, the flame is once again anchored at the backstep, with not only the number of triple flame points increasing but the most upstream triple flame point now moving closer to the dump plane. This phenomenon was similarly described in [24,33,52].

Figure B4 shows the HRR for the 9C case at four different times. The flame in this case is always weakly anchored at the dump plane. In contrast to case 14C, the number of triple flame points does not fluctuate. There is a lack of distinguishable triple flame points movement observed in case 14C. Immediately downstream of the backstep, the flame is predominantly premixed, as shown by the darker isocontour overlapping the high HRR regions.

Figure B5 shows the HRR for the 14CP case at four different times. The flame is now lifted away from the backstep. The number of triple flame points is now greatly reduced. There is no distinguishable movement of the triple flame point, which is similar to case 9C.

Although these time snapshots illustrate the FPV model ability to capture the correct physics, it also raises the importance of capturing the correct flame thickness. With the current mesh, most of the main physics are captured but the flame thicknesses are not completely resolved, leading to uncertainties in the flame dynamics analysis. Further investigation into this issue is needed.

Acknowledgments

This research was supported by the U.S. Air Force Office of Scientific Research under grant FA9550-15-1-0033, with Mitat Birkan as the Program Manager. Heinz Pitsch of RWTH Aachen University is acknowledged for providing us access to the FlameMaster code.

References

[1] Oefelein, J. C., and Yang, V., "Comprehensive Review of Liquid Propellant Combustion Instabilities in F-1 Engines," *Journal of Propulsion and Power*, Vol. 9, No. 5, 1993, pp. 657–677. doi:10.2514/3.23674

[2] Culick, F. E., and Yang, V., *Overview of Combustion Instabilities in Liquid-Propellant Rocket Engines*, Vol. 169, AIAA Progress in Astronautics and Aeronautics, AIAA, Washington, D.C., 1995, pp. 3–37, Chap. 1.

[3] Culick, F. E., "Unsteady Motions in Combustion Chambers for Propulsion Systems," AGARDograph AG-AVT-039, 2006.

[4] Sirignano, W. A., and Popov, P., "Two-Dimensional Model for Liquid-Rocket Transverse Combustion Instability," *AIAA Journal*, Vol. 51, No. 12, Dec. 2013, pp. 2919–2934. doi:10.2514/1.J052512

[5] Harrje, D., and Reardon, F., "Liquid Propellant Rocket Combustion Instability," NASA SP194, Jan. 1972.

[6] Crocco, L., and Cheng, S., "High Frequency Combustion Instability in Rockets with Distributed Combustion," *4th Symposium (International) on Combustion*, Vol. 4, No. 1, 1953, pp. 865–880. doi:10.1016/S0082-0784(53)80111-6

[7] Crocco, L., and Cheng, S., "Theory of Combustion Instability in Liquid Propellant Rocket Motors," AGARD Monograph 8, 1956.

[8] Sirignano, W. A., and Crocco, L., "A Shock Wave Model of Unstable Rocket Combustors," *AIAA Journal*, Vol. 2, No. 7, 1964, pp. 1285–1296. doi:10.2514/3.2534

[9] Mitchell, C. E., Crocco, L., and Sirignano, W. A., "Nonlinear Longitudinal Instability in Rocket Motors with Concentrated Combustion," *Combustion Science and Technology*, Vol. 1, No. 1, 1969, pp. 35–64. doi:10.1080/00102206908952190

[10] Poinsot, T. J., Trouve, A. C., Veynante, D. P., Candel, S. M., and Esposito, E. J., "Vortex-Driven Acoustically Coupled Combustion Instabilities," *Journal of Fluids Mechanics*, Vol. 177, April 1987, pp. 265–292. doi:10.1017/S0022112087000958

[11] Keller, J. O., Vaneveld, L., Korschelt, D., Hubbard, G. L., Ghoniem, A. F., Daily, J. W., and Oppenheim, A. K., "Mechanism of Instabilities in Turbulent Combustion Leading to Flashback," *AIAA Journal*, Vol. 20, No. 2, 1982, pp. 254–262. doi:10.2514/3.51073

[12] Lee, J. G., and Santavicca, D. A., "Experimental Diagnostics for the Study of Combustion Instabilities in Lean Premixed Combustors," *Journal of Propulsion and Power*, Vol. 19, No. 5, 2003, pp. 735–750. doi:10.2514/2.6191

[13] Sattelmayer, T., "Influence of the Combustor Aerodynamics on Combustion Instabilities from Equivalence Ratio Fluctuations," *Journal of Engineering for Gas Turbines and Power*, Vol. 125, No. 1, 2002, pp. 11–19. doi:10.1115/1.1365159

[14] Neumeier, Y., Zinn, B. T., and Jagoda, J. I., "Frequency Domain Analysis of the Performance of a Valved Helmholtz Pulse Combustor," *Combustion Science and Technology*, Vol. 94, Nos. 1–6, 1993, pp. 295–316. doi:10.1080/00102209308935316

[15] Lieuwen, T., and Zinn, B. T., "The Role of Equivalence Ratio Oscillations in Driving Combustion Instabilities in Low NOx Gas Turbines," *Symposium (International) on Combustion*, Vol. 27, No. 2, 1998, pp. 1809–1816. doi:10.1016/S0082-0784(98)80022-2

[16] Barr, P. K., Keller, J. O., Bramllette, T. T., Westbrook, C. K., and Dec, J. E., "Pulse Combustor Modeling Demonstration of the Importance of Characteristic Times," *Combustion and Flame*, Vol. 82, Nos. 3–4, 1990, pp. 252–269. doi:10.1016/0010-2180(90)90002-9

[17] Celik, I., Zhang, W., Spenik, J. L., and Morris, G. J., "One-Dimensional Modeling and Measurement of Pulsating Gas-Solid Flow in Tubes," *Combustion Science and Technology*, Vol. 94, Nos. 1–6, 1993, pp. 353–378. doi:10.1080/00102209308935319

[18] Popov, P. P., Sideris, A., and Sirignano, W. A., "Stochastic Modeling of Transverse Wave Instability in a Liquid-Propellant Rocket Engine," *Journal of Fluid Mechanics*, Vol. 745, April 2017, pp. 62–91. doi:10.1017/jfm.2014.96

[19] Popov, P. P., Sirignano, W. A., and Sideris, A., "Propellant Injector Influence on Liquid-Propellant Rocket Engine Instability," *Journal of Propulsion and Power*, Vol. 31, No. 1, 2015, pp. 320–331. doi:10.2514/1.B35400

[20] Menon, S., and Jou, W.-H., "Large-Eddy Simulations of Combustion Instability in an Axisymmetric Ramjet Combustor," *Combustion Science and Technology*, Vol. 75, Nos. 1–3, 1991, pp. 53–72. doi:10.1080/00102209108924078

[21] Staffelbach, G., Gicquel, L., Boudier, G., and Poinsot, T., "Large-Eddy Simulations of Self-Excited Azimuthal Modes in Annular Combustors," *Proceedings of the Combustion Institute*, Vol. 32, No. 2, 2009, pp. 2909–2916. doi:10.1016/j.proci.2008.05.033

[22] Ghani, A., Poinsot, T., Gicquel, L., and Staffelbach, G., "LES of Longitudinal and Transverse Self-Excited Combustion Instabilities in a Bluff-Body Stabilized Turbulent Premixed Flame," *Combustion and Flame*, Vol. 162, No. 11, 2015, pp. 4075–4083. doi:10.1016/j.combustflame.2015.08.024

[23] Srinivasan, S., Ranjan, R., and Menon, S., "Flame Dynamics During Combustion Instability in a High-Pressure, Shear-Coaxial Injector Combustor," *Flow, Turbulence and Combustion*, Vol. 94, No. 1, Jan. 2015, pp. 237–262. doi:10.1007/s10494-014-9569-x

[24] Harvazinski, M., Huang, C., Sankaran, V., Feldman, T., Anderson, W., Merkle, C., and Talley, D., "Coupling Between Hydrodynamics, Acoustics, and Heat Release in a Self-Excited Unstable Combustor," *Physics of Fluids*, Vol. 27, No. 4, 2015, Paper 045102. doi:10.1063/1.4916673

[25] Miller, K., Sisco, J., Nugent, N., and Anderson, W., "Combustion Instability with a Single Element Swirl Injector," *Journal of Propulsion and Power*, Vol. 23, No. 5, 2007, pp. 1102–1112. doi:10.2514/1.26826

[26] Yu, Y. C., Koeglmeier, S. M., Sisco, J. C., and Anderson, W. E., "Combustion Instability of Gaseous Fuels in a Continuously Variable Resonance Chamber (CVRC)," *44th AIAA/ASME/SAE/ASEE Joint Propulsion Conference and Exhibit*, AIAA Paper 2008-4657, July 2008. doi:10.2514/6.2008-4657

[27] Yu, Y. C., O'Hara, L., Sisco, J. C., and Anderson, W. E., "Experimental Study of High-Frequency Combustion Instability in a Continuously Variable Resonance Combustor(CVRC)," *47th AIAA Aerospace Sciences Meeting Including the New Horizons Forum and Aerospace Exposition*, AIAA Paper 2009-0234, 2009. doi:10.2514/6.2009-234

[28] Yu, Y. C., Sisco, J. C., Rosen, S., Madhav, A., and Anderson, W. E., "Spontaneous Longitudinal Combustion Instability in a Continuously Variable Resonance Combustor," *Journal of Propulsion and Power*, Vol. 28, No. 5, 2012, pp. 876–887. doi:10.2514/1.B34308

[29] Garby, R., Selle, L., and Poinsot, T., "Large-Eddy Simulation of Combustion Instabilities in a Variable Length Combustor," *Comptes Rendus Mecanique*, Vol. 341, Nos. 1–2, 2013, pp. 220–229. doi:10.1016/j.crme.2012.10.020

[30] Harvazinski, M. E., Anderson, W. E., and Merkle, C. L., "Analysis of Self-Excited Combustion Instabilities Using Two- and Three Dimensional Simulations," *Journal of Propulsion and Power*, Vol. 29, No. 2, 2013, pp. 396–409. doi:10.2514/1.B34732

[31] Harvazinski, M. E., Talley, D. G., and Sankaran, V., "Application of Detailed Chemical Kinetics to Combustion Instability Modeling," *54th AIAA Aerospace Sciences Meeting*, AIAA Paper 2016-1931, Jan. 2016. doi:10.2514/6.2016-1931

[32] Harvazinski, M., Sankaran, V., and Talley, D., "Parametric Trends in the Combustion Stability Characteristics of a Single-Element Gas-Gas Rocket Engine," *52nd AIAA Aerospace Sciences Meeting*, AIAA Paper 2014-0577, Jan. 2014. doi:10.2514/6.2014-0577

[33] Sardeshmukh, S. V., Heister, S. D., and Anderson, W. E., "Prediction of Combustion Instability with Detailed Chemical Kinetics," *53rd AIAA Aerospace Sciences Meeting*, AIAA Paper 2015-1826, Jan. 2015. doi:10.2514/6.2015-1826

[34] Spalart, P., Jou, W. H., Strelets, M., and Allmaras, S., "Comments on the Feasibility of LES for Wings and on a Hybrid RANS/LES Approach," *1st AFOSR Conference on DNS/LES*, Greyden Press, Columbus, OH, Jan. 1997, pp. 137–147.

[35] Pecnik, R., Terrapon, V. E., Ham, F., Iaccarino, G., and Pitsch, H., "Reynolds-Averaged Navier–Stokes Simulations of the Hyshot II Scramjet," *AIAA Journal*, Vol. 50, No. 8, 2012, pp. 1717–1732. doi:10.2514/1.J051473

[36] Wilcox, D. C., *Turbulence Modelling for CFD*, 3rd ed., D.C.W. Industries, La Cañada, CA, 2006, pp. 255–256.

[37] Strelets, M., "Detached Eddy Simulation of Massively Separated Flows," *39th Aerospace Sciences Meeting and Exhibit*, AIAA Paper 2001-0879, Jan. 2001. doi:10.2514/6.2001-879

[38] Peters, N., *Turbulent Combustion*, 2nd ed., Cambridge Monographs on Mechanics, Cambridge Univ. Press, Cambridge, England, U.K., 2000, pp. 42–53.

[39] Pierce, C. D., and Moin, P., "Progress-Variable Approach for Large-Eddy Simulation of Non-Premixed Turbulent Combustion," *Journal of Fluid Mechanics*, Vol. 504, April 2004, pp. 73–97. doi:10.1017/S0022112004008213

[40] Saghafian, A., Shunn, L., Phillip, D. A., and Ham, F., "Large Eddy Simulations of the HIFiRE Scramjet Using a Compressible Flamelet/Progress Variable Approach," *Proceedings of the Combustion Institute*, Vol. 35, No. 2, 2015, pp. 2163–2172. doi:10.1016/j.proci.2014.10.004

[41] Wang, H., Piao, Y., and Niu, J., "IDDES Simulation of Supersonic Combustion Using Flamelet Modeling," *22nd AIAA Computational Fluid Dynamics Conference*, AIAA Paper 2015-3211, June 2015. doi:10.2514/6.2015-3211

[42] Jameson, A., Schmidt, W., and Turkel, E., "Numerical Solution of the Euler Equations by Finite Volume Methods Using Runge Kutta Time Stepping Schemes," *14th Fluid and Plasma Dynamics Conference*, AIAA Paper 1981-1259, June 1981. doi:10.2514/6.1981-1259

[43] Hoffmann, K. A., and Chiang, S. T., *Computational Fluids Dynamics*, Vol. 2, 4th ed., Engineering Education System, Wichita, KS, 2000, pp. 275–276.

[44] Poinsot, T., and Veynannte, D., *Theoretical and Numerical Combustion*, 2nd ed., R.T. Edwards Inc., Philadelphia, PA, 2005, pp. 431–452.

[45] Crocco, L., and Sirignano, W. A., "Effects of Transverse Velocity Components on the Nonlinear Behavior of Short Nozzles," *AIAA Journal*, Vol. 4, No. 8, 1966, pp. 1428–1430. doi:10.2514/3.3691

[46] Pitsch, H., "FlameMaster, A C++ Computer Program for 0D Combustion and 1D Laminar Flame Calculations," Ver. V.3.3.10, https://www.itv.rwth-aachen.de/index.php?id=request#c957 [retrieved 18 March 2015].

[47] Peters, N., and Rogg, B., *Reduced Kinetic Mechanism for Applications in Combustion System*, Lecture Notes in Physics, Springer–Verlag, Berlin, 1993, pp. 6–12.

[48] Harvazinski, M., "Modeling Self-Excited Combustion Instabilities Using a Combination of Two and Three Dimensional Simulations," Ph.D. Thesis, Purdue Univ., West Lafayette, IN, May 2012.

[49] Wu, H., Ma, P. C., Lv, Y., and Ihme, M., "MVP-Workshop Contribution: Modeling of Volvo Bluff Flame Experiment," *55th AIAA Aerospace Sciences Meeting*, AIAA Paper 2017-1573, Jan. 2017. doi:10.2514/6.2017-1573

[50] Comer, A. L., Sardeshmukh, S., Rankin, B. A., Harvazinski, M. E., and Sankaran, V., "Grid Convergence Studies of Bluff Body Stabilized Turbulent Premixed Combustion," *55th AIAA Aerospace Sciences Meeting*, AIAA Paper 2017-0377, Jan. 2017. doi:10.2514/6.2017-0377

[51] Weinman, K. A., van der Ven, H., Mockett, C. R., Knopp, T. A., Kok, J. C., Perrin, R. T., and Thiele, F. H., "A Study of Grid Convergence Issues for the Simulation of the Massively Separated Flow Around a Stalled Airfoil Using DES and Related Method," *European Conference on Computational Fluid Dynamics*, Delft Univ. of Technology, Egmond aan Zee, The Netherlands, Jan. 2006, pp. 1–26.

[52] Guezennec, N., Dawson, T., Sierra, P., and Menon, S., "Flame Holding Dynamics During Combustion Instability in a Shear-Coaxial Injector Combustor," *International Symposium on Turbulence and Shear Flow Phenomena*, Turbulence and Shear Flow Phenomena (TSFP), Portiers, France, Aug. 2013.

[53] Schadow, K., and Gutmark, E., "Combustion Instability Related to Vortex Shedding in Dump Combustors and Their Passive Control," *Progress in Energy and Combustion Science*, Vol. 18, No. 2, 1992, pp. 117–132. doi:10.1016/0360-1285(92)90020-2

[54] Popp, S., Hunger, F., Hartl, S., Messig, D., Coriton, B., Frank, J. H., Fuest, F., and Hasse, C., "LES Flamelet-Progress Variable Modeling and Measurements of a Turbulent Partially-Premixed Dimethyl Ether Jet Flame," *Combustion and Flame*, Vol. 162, No. 8, 2015, pp. 3016–3029. doi:10.1016/j.combustflame.2015.05.004

[55] Renzoa, M. D., Coclitea, A., de Tullioa, M. D., Palmaa, P. D., and Pascazioa, G., "LES of the Sandia Flame D Using an FPV Combustion Model," *Energy Procedia*, Vol. 82, 2015, pp. 402–409. doi:10.1016/j.egypro.2015.11.824

J. M. Seitzman
Associate Editor